nature communications

Article

https://doi.org/10.1038/s41467-025-62852-1

Single-molecule tweezers decode hidden dimerization patterns of membrane proteins within lipid bilayers

Received: 8 March 2025

Accepted: 29 July 2025

Published online: 09 August 2025

Check for updates

Victor W. Sadongo[1,5], Eojin Kim[1,5], Seoyoon Kim[1,5], W. C. Bhashini Wijesinghe[1], Taeseung Lee[2,3], Jeong-Mo Choi[2,3] & Duyoung Min[1,4]

Dimerization of transmembrane (TM) proteins is a fundamental process in cellular membranes, central to numerous physiological and pathological pathways, and increasingly recognized as a promising therapeutic target. Although often described as a simple two-state transition from monomers to dimers, the process following monomer diffusion—referred to as post-diffusion dimerization—is likely more intricate due to complex inter-residue interactions. Here, we present a single-molecule tweezer platform that directly profiles these post-diffusion transitions during TM protein dimerization. This approach captures reversible dimerization events of individual TM dimers, revealing previously hidden intermediate states that emerge after monomer diffusion. By integrating measurements of intermediates, kinetics, and energy landscapes with molecular dynamics simulations, we delineate the dimerization pathway and dissect how residue interactions and lipid bilayers influence the process. Furthermore, our platform allows for the targeted analysis of localized perturbations—such as those induced by peptide binding or site-directed mutagenesis—demonstrating its utility for probing the mechanisms of TM dimer-targeting therapeutics at single-molecule resolution.

Dimerization of transmembrane (TM) proteins is a fundamental biological event within lipid bilayers, essential for regulating protein function and transducing signals across membranes[1–7]. This process underlies critical cellular activities, such as growth factor signaling through receptor tyrosine kinases, cell fate control during organogenesis via Notch receptors, and cell adhesion mediated by integrins and cadherins[4,6,8–11]. Disrupting or modulating TM protein dimerization has emerged as a promising therapeutic strategy for treating diseases like cancer and immune disorders[1,12–16]. For example, monoclonal antibodies have been developed to inhibit dimerization of the epidermal growth factor receptor (EGFR) family, effectively blocking downstream signaling and tumor progression[17–20]. Additionally, anti-TM domain peptides—such as computed helical anti-membrane proteins (CHAMPs)—have been engineered to disrupt TM dimer formation across a range of targets, including cytokine receptors, integrins, and G protein-coupled receptors (GPCRs)[1,12,14,15,21–25].

Various experimental approaches—including molecular chimera assays with dimerization reporters, fluorescence-based techniques, and steric trapping—have identified interaction motifs involved in TM protein dimerization, characterized their thermodynamic stabilities across different membrane environments, and elucidated key mechanistic insights into the dimerization process[2,3,5,26–40]. However, the details of the molecular events that occur after monomer diffusion within lipid bilayers—the post-diffusion dimerization process—remain poorly understood (Fig. 1). The commonly used two-state model, which assumes a direct transition from monomeric to fully dimerized

[1]Department of Chemistry, Ulsan National Institute of Science and Technology, Ulsan, Republic of Korea. [2]Department of Chemistry, Pusan National University, Busan, Republic of Korea. [3]Chemistry Institute for Functional Materials, Pusan National University, Busan, Republic of Korea. [4]X-Dynamic Research Center, Ulsan National Institute of Science and Technology, Ulsan, Republic of Korea. [5]These authors contributed equally: Victor W. Sadongo, Eojin Kim, Seoyoon Kim. e-mail: dymin@unist.ac.kr

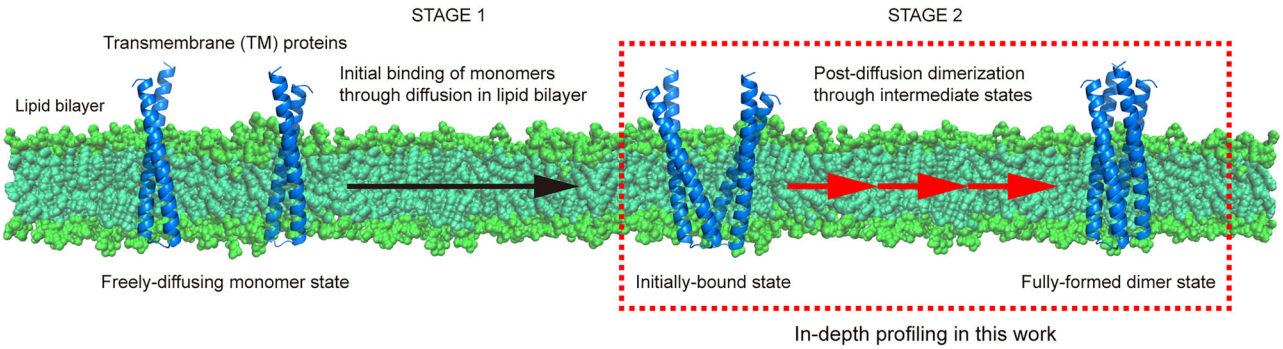

Fig. 1 | Dimerization process of transmembrane (TM) proteins. The dimerization process of transmembrane (TM) proteins can be divided into two stages: (1) the free diffusion of TM monomers within a lipid bilayer and their initial binding, and (2) the formation of dimers through intermediate states, *i.e.*, the post-diffusion dimerization. This study focuses on the second stage, highlighted by the red dashed box, and investigates it in depth using single-molecule tweezers and molecular dynamics simulations. The protein structures shown represent TMHC2, a designed TM homodimer used as a model protein in this work.

TM proteins, likely oversimplifies the actual process. For instance, recent computational studies suggest that TM dimerization follows rugged energy landscapes involving multiple intermediate states[41–46]. Moreover, as many drug molecules are designed to target specific residue-level interactions, a detailed understanding of the post-diffusion transition dynamics is crucial.

In this work, we present a single-molecule platform specifically designed to study TM protein interactions within lipid bilayers—unlike previous single-molecule force spectroscopy (SMFS) approaches, which primarily focused on interactions between soluble domains or proteins[47–61] (see Discussion for details). Our platform enables detailed profiling of post-diffusion events during TM protein dimerization, revealing hidden intermediate states, transition kinetics, and the underlying dimerization energy landscape beyond the initial monomer diffusion step. It also captures how peptide inhibition and site-directed mutagenesis modulate dimerization patterns and stability. Together, our single-molecule method provides a powerful tool for dissecting the complexity of TM protein dimerization and interactions, particularly in biologically and pharmaceutically relevant systems such as receptor tyrosine kinases and cytokine receptors.

Results

Single-molecule tweezer platform for studying TM dimer dissociation and dimerization

We established our single-molecule tweezer system using a designed TM homodimer, TMHC2 (Fig. 2a, b, Supplementary Figs. 1–4, and Methods). Each TMHC2 monomer comprises two TM helices forming a helical hairpin structure[62] (Fig. 2a and Supplementary Fig. 4a, b). TMHC2 was selected as a model system for two main reasons. First, it offers experimental tractability—its single-chain variant was recently shown to be a robust model for single-molecule tweezer studies of TM protein (un)folding[63]. Second, it holds physiological relevance—its TM domain assembles via leucine zipper-like interactions (Supplementary Fig. 4a, b), a common motif found in biologically significant TM dimers such as receptor tyrosine kinases, cytokine receptors, and cadherins[1,64–69].

To apply force to a single TM dimer, the N-termini of its constituent monomers were tethered to a glass surface and a magnetic bead, respectively, via ~1 kbp DNA handles using orthogonal conjugation strategies, including DBCO-azide click chemistry, SpyCatcher-SpyTag binding, and traptavidin-2×biotin binding[63,70] (Fig. 2b and Methods). To prevent permanent dissociation, the N-termini were also linked by an elastin-like polypeptide (ELP) linker that lacks secondary structures, using SnoopCatcher-SnoopTag binding (Fig. 2b, Supplementary Figs. 1–3, and Methods). The ELP linker enables repeated observation of dimerization events following force-induced dissociation (Fig. 2c; see below for details). We used ELP linkers of varying lengths—75, 111, and 146 amino acids (ELP-S, -M, and -L, respectively; Fig. 2d and Supplementary Fig. 1)—resulting in distinct dissociation step sizes, as predicted by the worm-like chain (WLC) model (Fig. 2e). The SnoopCatcher (engineered with a properly positioned disulfide knot) and SpyCatcher proteins form covalent complexes with their respective peptide tags and remain folded under applied force[63,70,71] (Supplementary Fig. 3). The lipid bilayer environment was reconstituted using bicelles—disc-shaped lipid bilayers encircled by detergents (Fig. 2b and Methods).

We employed two experimental modes: force-ramp (Fig. 2c) and force-clamp (Fig. 2f). In the force-ramp mode, where the applied force is gradually increased and then relaxed in cycles, we assessed the overall patterns of dissociation and dimerization (Fig. 2c). For example, this mode allowed us to verify whether dimer dissociation conformed to the expected behavior based on ELP linker extension (Fig. 2d, e). We then used the force-clamp mode, in which a constant force is applied, to examine potential intermediate states during dissociation or dimerization (Fig. 2f). Under constant force, the WLC model predicts uniform step sizes (Fig. 2e), albeit with thermal fluctuations, enabling quantitative analysis of these intermediate states.

Repetitive dissociation and dimerization of a single TM dimer within lipid bilayers

In the force-ramp mode, the gradual application of force dissociated single TM dimers into monomers, primarily at 20–40 pN, as indicated by stepwise increases in molecular extension due to ELP linker stretching (Fig. 3a and Supplementary Fig. 5). As expected, the dissociation step size (~10–40 nm) increased with ELP linker length, consistent with predictions from the WLC model[72] (Fig. 3a, b, Supplementary Fig. 5, and Methods). Subsequent relaxation of the force back to 1 pN induced dimer reformation (Fig. 3a), with a high efficiency of 97–99% across repeated force cycles (Fig. 3c and Methods). In these experiments, dimerization occurred at low force levels (<10 pN), where step sizes decreased to below ~20 nm (Fig. 3a). Across all ELP linker lengths, the observed dissociation and dimerization step sizes (~10–40 nm) remained within the diameter of lipid bilayer discs (~50 nm) (Fig. 3b and Supplementary Figs. 5, 6), supporting the conclusion that these transitions occurred within a lipid bilayer environment.

Buffer exchange experiments—in which the buffer containing lipid bilayer discs was replaced with one lacking any lipid or detergent molecules (see Methods for detailed procedures and compositions)—provided additional evidence that the observed dissociation and dimerization events occur within a lipid bilayer. After the buffer exchange, dissociation events were no longer observed, indicating that re-dimerization into the native form did not occur in the absence of lipid bilayers (Fig. 3d and Supplementary Fig. 7). Although the

https://doi.org/10.1038/s41467-025-62852-1

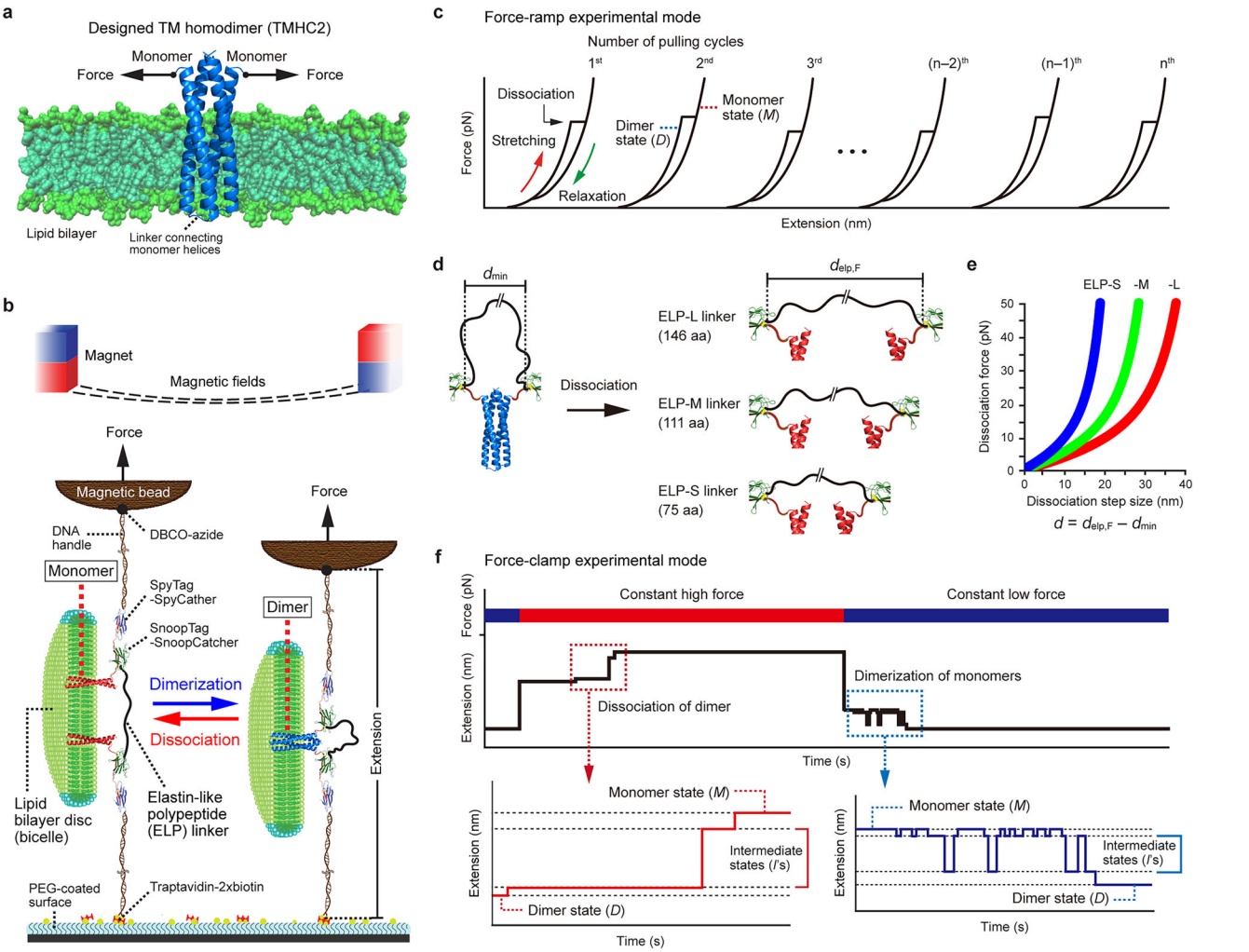

Fig. 2 | Schematic overview of our single-molecule tweezers and experimental modes. a Designed transmembrane (TM) homodimer TMHC2 as a model protein used in this study. The direction of applied mechanical force is indicated by arrows. **b** Our single-molecule tweezer platform. Monomers are connected by an elastin-like polypeptide (ELP) linker, enabling repeated observation of dimer dissociation and re-dimerization. **c** Force-ramp experimental mode, in which the force is gradually increased and relaxed in cycles, used to assess the overall patterns of dissociation and dimerization. This mode allows rapid verification of whether dimer dissociation follows the expected behavior based on ELP linker stretching. **d** Schematic of dimer dissociation with varying ELP linker lengths. The dimer structure size and the ELP linker extension under force are denoted as d_{min} and $d_{elp,F}$, respectively. **e** Expected dissociation force and step size for each ELP linker, estimated using the worm-like chain (WLC) model. The dissociation step size (d) corresponds to the ELP linker extension under force, corrected for the size of the dimer structure ($d = d_{elp,F} - d_{min}$). **f** Force-clamp experimental mode, in which a constant force is applied to analyze potential intermediate states during dissociation or dimerization. Under constant force, the WLC model predicts a consistent level of step sizes, enabling quantitative characterization of intermediate states.

hydrophobic TM segments may still engage in nonspecific interactions under these conditions at low forces, such non-native associations are likely unstable and readily disrupted, thus failing to generate the high-force dissociation steps characteristic of the stable native dimer.

Identifying hidden intermediate states in TM dimer dissociation and dimerization

In the force-ramp experiments, potential dissociation intermediates may have been obscured by rapid and cooperative transitions induced by high force levels. We therefore employed force-clamp experiments at constant lower forces to slow transitions and reveal potential intermediate states (Fig. 4a, b). At 20 pN, the majority of the traces (~70%) exhibited single-step dissociation, whereas the remaining ~30% showed two or three steps involving two distinct intermediate states (Fig. 4a, c and Supplementary Fig. 8a). A Cys mutant—with a disulfide bond linking the N- and C-termini of each monomer—displayed a similar dissociation pattern (Fig. 4b, d and Supplementary Fig. 8b), excluding the possibility of helix dissociation within individual monomers. These results suggest that the observed intermediates arise from inter-monomer interactions rather than intra-chain interactions within a monomer, consistent with our pulling design, which does not separate the helices within each monomer. The pulling geometry further constrains the dissociation pathway to proceed directionally, from the pulling side toward the opposite side.

Previous single-molecule forced unfolding studies have shown that helix–coil transitions can occur at ~18 pN in membrane proteins, including a single-chain variant of TMHC2[63,73]. Thus, the intermediate dissociation steps observed at the constant force of 20 pN may have been accompanied by structural denaturation from helices to polypeptides. In contrast, once fully dissociated, the monomers are no longer under external force, allowing any unstructured regions to refold into helical structures. Thus, dimerization is expected to initiate from structured monomers, leading to a uniform dimer structure. This interpretation is further supported by the highly monodisperse distributions of dissociation forces and step sizes observed in our experiments (Supplementary Fig. 5). If the dimers were structurally

https://doi.org/10.1038/s41467-025-62852-1

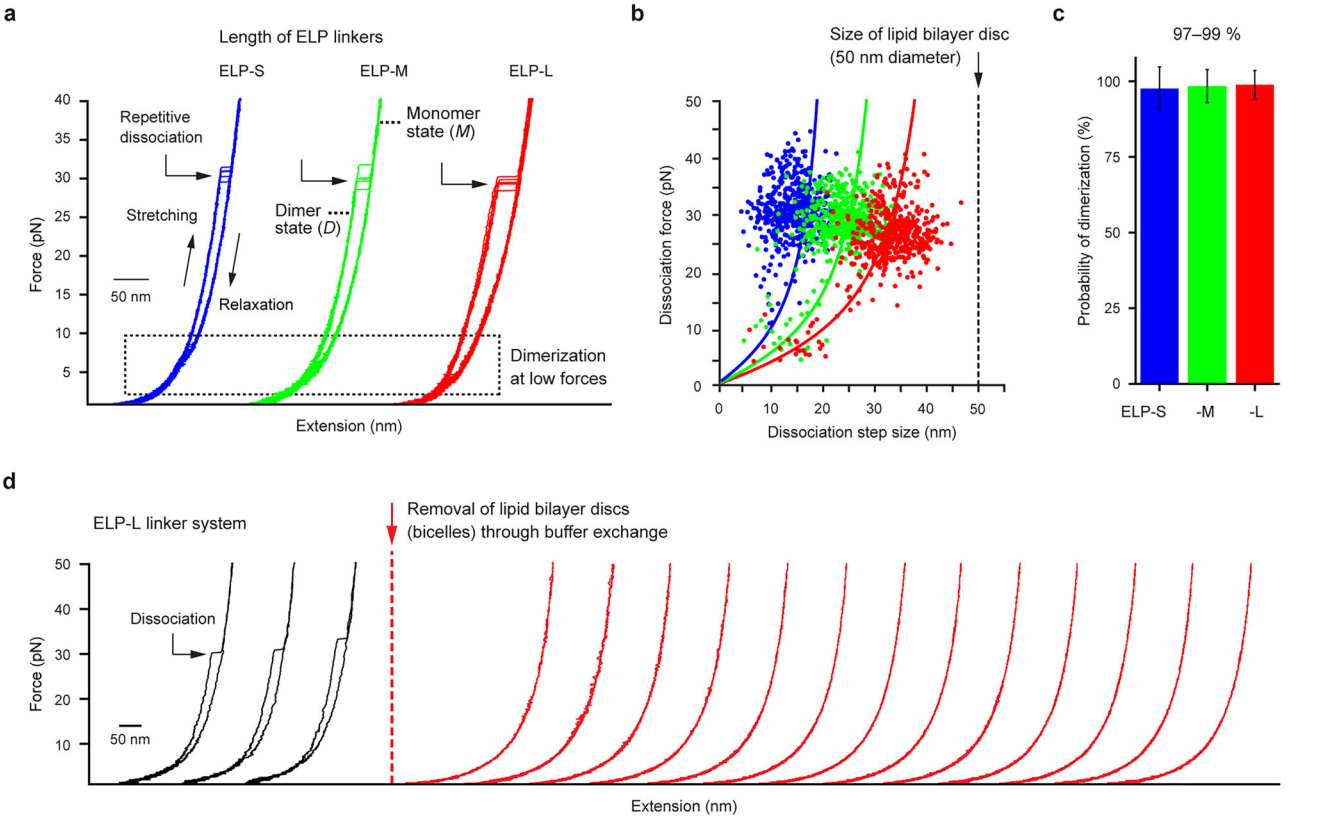

Fig. 3 | Repetitive dissociation and dimerization of a single TM dimer within lipid bilayers. a Force-extension curves showing repetitive dissociation events of a single TMHC2 during force-ramp experiments, where the force is gradually applied and released. The black dashed box highlights the force range for re-dimerization after dissociation. **b** Scatter plots of dissociation forces and step sizes ($n = 500$ data points from 5 molecules for each ELP linker system; i.e., each molecule was subjected to 100 pulling cycles). The data are analyzed using the worm-like chain model (curved lines). All step sizes are smaller than the diameter of lipid bilayer discs (bicelles; 50 nm). **c** Probability of dimerization in the force-ramp experiments ($n = 500$ traces from 5 molecules for each ELP linker system; mean ± SD). **d** Force-extension curves before and after the removal of lipid bilayer discs through buffer exchange (shown in black and red, respectively).

heterogeneous or partially disordered, we would expect highly broad or polydisperse distributions, as seen under peptide-binding or site-directed mutagenesis conditions (see relevant sections below). Accordingly, we focused our analysis on the dimerization phase, which enables unambiguous mapping of intermediate states without the confounding effects of potential helix denaturation.

To this end, we reduced the force to a much lower range of 5–13 pN to induce dimerization, following complete dissociation at 35 pN (Fig. 5a and Supplementary Fig. 9). At these low forces, transitions between different extension levels occurred frequently but were difficult to resolve due to high fluctuation noise from the tethered bead (Fig. 5a and Supplementary Figs. 10–13). To address this, we applied hidden Markov modeling (HMM) in combination with the Bayesian information criterion (BIC), which enabled the identification of four distinct states: monomer (M), intermediate 1 (I_1), intermediate 2 (I_2), and dimer (D) (Fig. 5a, Supplementary Figs. 14–16, and Methods). Even at forces of 5–13 pN, 84–86% of traces showed full dimerization to the D state, consistently following the sequence $M \rightarrow I_1 \rightarrow I_2 \rightarrow D$ with few bypasses (Fig. 5b, Supplementary Fig. 17, and Supplementary Table 1). The total step sizes for dimerization (~10–20 nm) remained within the diameter of lipid bilayer discs (~50 nm) (Fig. 5c and Supplementary Figs. 15, 6), consistent with the in-bilayer transitions discussed above.

The pulling geometry constrains dimerization to proceed along a specific pathway—from the side opposite the pulling point to the pulling side—*i.e.*, the reverse of dissociation. Nevertheless, our experimental design captures the predominant dimerization pathway even in the absence of external force (see subsequent sections for details). When the extension levels of the M and D states were normalized to 0 and 1, respectively, the I_1 and I_2 states corresponded to ~0.2 and ~0.8 on average (Fig. 5d and Supplementary Fig. 18). These intermediate positions closely matched those observed during dimerization of the Cys mutant (Fig. 5d and Supplementary Fig. 18), indicating that I_1 and I_2 arise from inter-monomer interactions and represent ~20% and ~80% dimer formation, respectively. The intermediate positions identified during dimerization were also similar to those observed during dissociation of the wild-type (Fig. 5d), suggesting that the residue positions involved in intermediates states are comparable in both directions of the transition.

Structural mapping of dimerization intermediate states

To investigate the structures of the intermediate states (Fig. 5e–j and Methods), we designated the leucine zipper-like, closely interacting inner residues at the dimerization interface as the 1st to 10th interaction layers, spaced every 3–4 residues from the opposite side to the pulling side (Fig. 5e, f and Supplementary Fig. 4a, b). The flexible polypeptide linkers connecting the monomer helices were also designated as the 0th interaction layer, as their flexibility allows close inter-monomer contact. Based on the directionality of dimerization (from the 0th to the 10th layer), the I_1 and I_2 states—corresponding to ~20% and ~80% dimer formation—approximately align with dimerization up to the 2nd and 8th layers, respectively (Fig. 5e, f and Supplementary Fig. 4a, b). This structural mapping of intermediates, combined with all-atom molecular dynamics (AAMD) simulations, delineates three distinct domains (Fig. 5h, i and Methods): edge TM domain ($D_{\text{TM-edge}}$, 0th–2nd layers), core TM domain ($D_{\text{TM-core}}$, 2nd–8th layers), and soluble domain (D_{soluble}, 8th–10th layers). The

https://doi.org/10.1038/s41467-025-62852-1

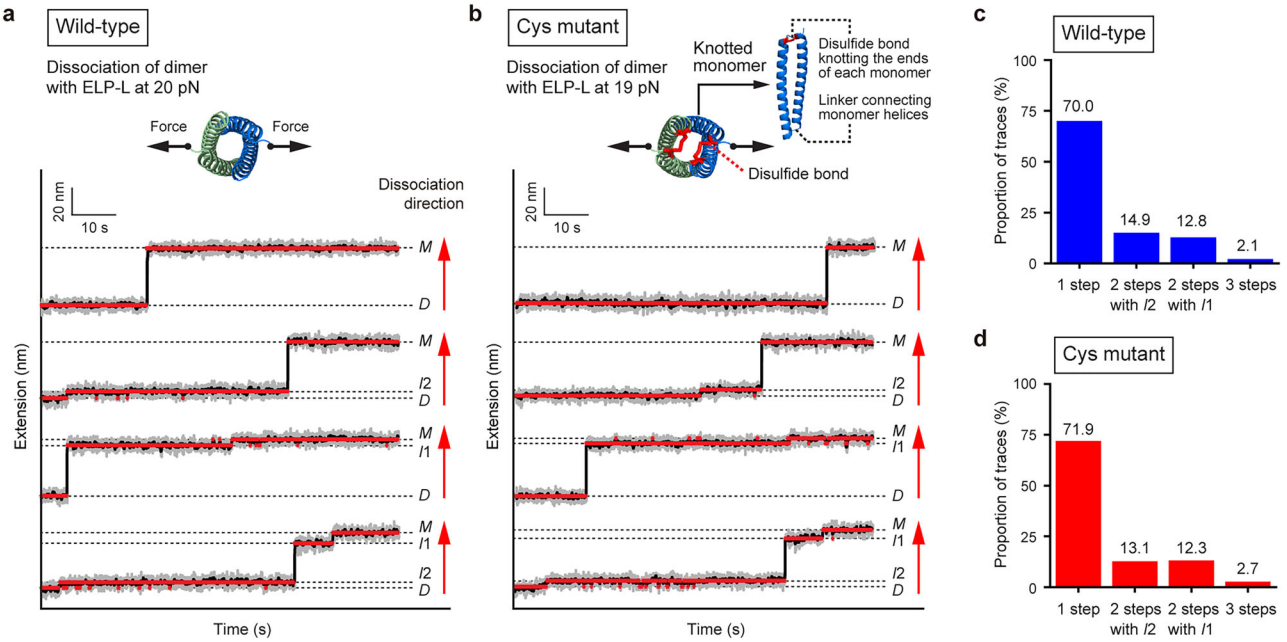

Fig. 4 | Intermediate states in TM dimer dissociation. a, **b** Time-resolved extension traces showing the dissociation of wild-type TMHC2 (**a**) and its Cys mutant (**b**) during force-clamp experiments, where the force is held constant. The dimer state (*D*) transitions to the monomer state (*M*) via intermediate states (I_2, I_1, or both). In the Cys mutant, the N- and C-terminal ends of each monomer are knotted by a disulfide bond, shown in red. The gray, black, and red traces represent raw traces, median-filtered traces, and traces identified using a hidden Markov model, respectively. Red arrows indicate the direction of dissociation from the *D* to *M* state. **c**, **d** Proportion of traces in each classification category for wild-type TMHC2 (**c**) and its Cys mutant (**d**) during the force-clamp experiments.

dimerization pathway thus proceeds via the sequential association of the $D_{\text{TM-edge}}$, $D_{\text{TM-core}}$, and D_{soluble} domains (Fig. 5j).

Using AAMD simulations and the residue interaction network generator (RING)[70,74,75] (Methods), we further examined how specific inter-monomer interactions correlate with the positions of intermediate states (Fig. 5g, h). Van der Waals interactions (F_{vdw}) were broadly distributed across the layers, with prominent peaks in the 3rd–4th and 7th–8th layer regions (Fig. 5g and Supplementary Fig. 19). Other intermolecular forces were more spatially localized: hydrogen bonding ($F_{\text{H-bond}}$) was enriched in the 0th–1st and 8th–9th layer regions, while ionic interactions (F_{ionic}) were concentrated in the 8th–9th layer region. This AAMD-RING analysis suggests that intermediate states emerge at positions where specific residue interactions change significantly—i.e., the transition from $F_{\text{H-bond}}$ to F_{vdw} around the 2nd layer and the sharp emergence of $F_{\text{H-bond}}$ and F_{ionic} around the 8th layer (Fig. 5g). In contrast, these intermediate positions do not strictly correlate with solvent boundaries: the 8th layer lies at the lipid headgroup-water interface, whereas the 2nd layer is embedded within the hydrophobic lipid tail region (Fig. 5h).

The spatial correlation between the positions of dimerization intermediates and the sharp transitions in intermolecular forces is unlikely to be coincidental. Moreover, peptide-binding experiments targeting the region near the I_2 state substantially altered the local dimerization energy landscape at that site (see relevant section below). Taken together, these independent lines of evidence reinforce the validity of our intermediate state analysis.

Our method captures the predominant dimerization pathway under force-free conditions

The natural dimerization process, in the absence of external forces, is not necessarily confined to a specific pathway—such as the 0th-to-10th layer dimerization discussed above. To assess whether our method captures the predominant pathway under force-free conditions, we conducted coarse-grained MD (CGMD) simulations using the Martini model for two initial configurations (Fig. 6a and Methods): (1) an initial monomer system, in which unbound monomers were initially separated by ~10 nm within a lipid bilayer to allow free diffusion and dimer formation, and (2) an initial dimer system, in which a dimer was preformed and used as a control. To confirm stable dimer formation in the monomer system, we calculated the root mean square deviation (RMSD) from the final protein structure at 2 μs for both systems (Fig. 6b). After dimer formation (see Methods for criteria), the RMSDs were comparable between the two systems, indicating that the monomers had successfully and stably formed dimers (Fig. 6c).

We then quantified the dimerization process following monomer diffusion—*i.e.*, the post-diffusion dimerization (Methods). After diffusion, the dimerization percentage rapidly increased from 0% to 100% (Fig. 6d, e). During this phase, time-resolved binding profiles were monitored for the 0^{th}–10^{th} interaction layers (Fig. 6f and Supplementary Fig. 20). Across 80 simulations that resulted in dimer formation, a statistically predominant binding order emerged, proceeding sequentially from the 0^{th} to 10^{th} layer (Fig. 6g). This binding order was further supported by quantitative analyses of the first binding time and total bound-state duration (Fig. 6h, i and Supplementary Fig. 21). The directional binding is likely driven by asymmetric solvation of the hydrophilic interaction layers within the hydrophobic lipid membrane—specifically, the 0^{th}–1^{st} layers likely serve as nucleation points due to their strong hydrogen bonding capacity in the membrane environment (Fig. 5f–h). These results suggest that our single-molecule tweezer method captures transitions along the predominant dimerization pathway (from the 0^{th} to the 10^{th} layer) even in the absence of external forces.

Mapping post-diffusion kinetics and energy landscape in TM protein dimerization

We revisited the single-molecule experimental data to estimate the post-diffusion kinetics and energetics of dimerization transitions under zero-force conditions (Fig. 7, Supplementary Table 2, and Methods). Using the Bell-Evans model[72], we extrapolated the force-dependent rate constants for each dimerization domain (k_a for association, k_d for dissociation) to obtain the zero-force rate constants (k_0)

https://doi.org/10.1038/s41467-025-62852-1

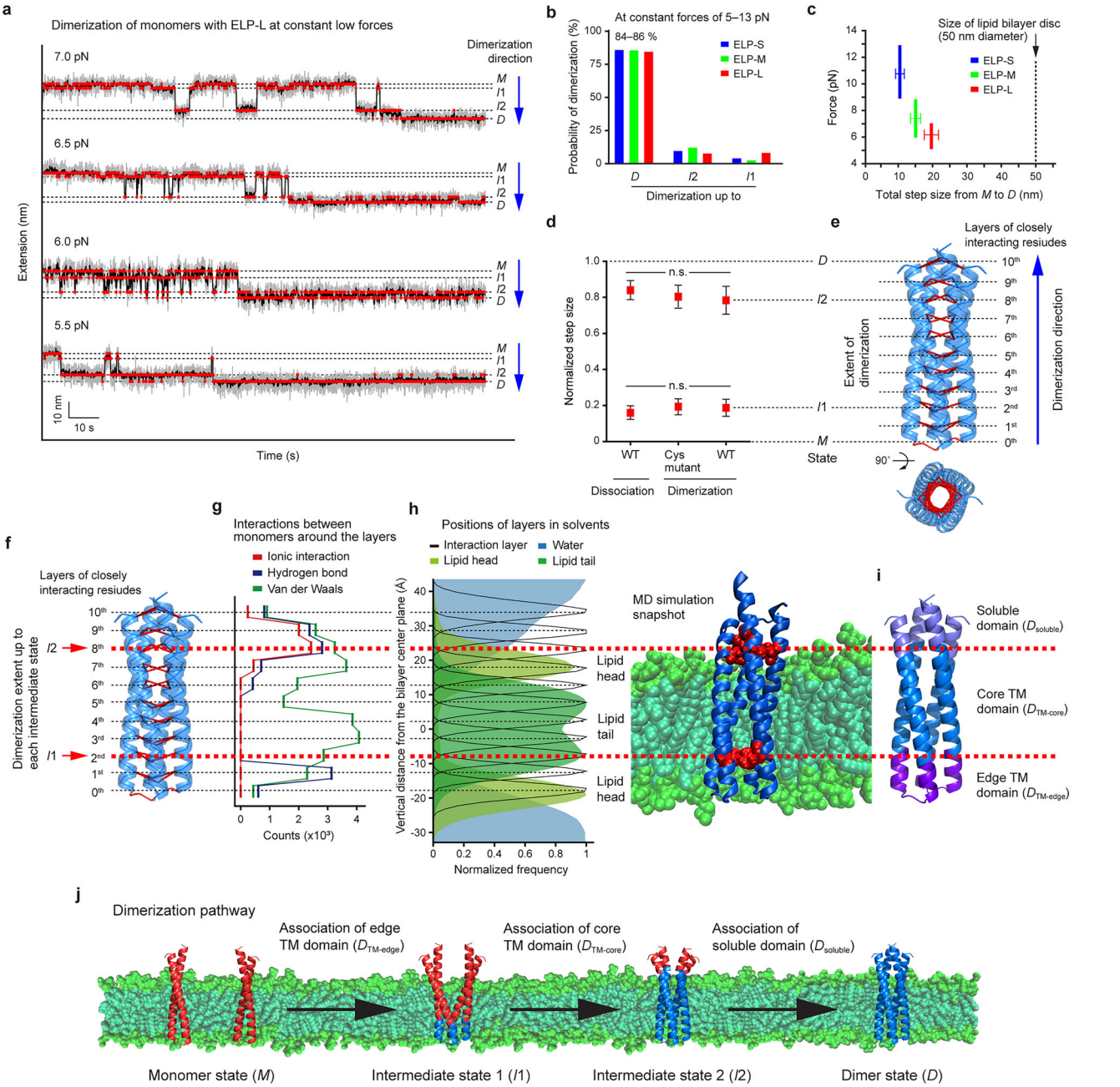

Fig. 5 | Intermediate states in TM protein dimerization. a Time-resolved extension traces showing dimerization events of a single TMHC2 during force-clamp experiments, where the force is held constant. The monomer state (*M*) transitions to the dimer state (*D*) via two intermediate states (I_1 and I_2). The gray, black, and red traces represent raw traces, median-filtered traces, and traces identified using a hidden Markov model, respectively. Blue arrows indicate the direction of dimerization from the *M* to *D* state. **b** Probability of dimerization up to each state in the force-clamp experiments ($n = 224–358$ traces from 8–13 molecules). **c** Distribution of total step sizes from the *M* to *D* state (mean ± SD; $n = 238$, 150, and 142 data points from 13, 8, and 13 molecules for EPL-S, -M, and -L systems, respectively). All step sizes are smaller than the diameter of lipid bilayer discs (bicelles; 50 nm). **d** Normalized step sizes for the intermediates. The data are presented as mean ± SD (right, $n = 530$ data points from 34 molecules in all ELP systems at 5–13 pN; middle, $n = 59$ data points from 3 molecules in the ELP-L system at 5–7 pN; left, $n = 7$ (I_1) and 9 (I_2) data points from 3 molecules in the ELP-L system at 20 pN). One-way ANOVA with post-hoc Tukey HSD test (n.s. for $p > 0.05$). **e**, **f** TMHC2 dimer structure showing the layers of closely interacting inner residues at the dimerization interface. The normalized step sizes of the intermediates in **d** are compared to the extent of dimerization from the 0th to 10th layer in **e**. **g** Counts of inter-monomer interactions around the interaction layers. This data was obtained using RING and all-atom molecular dynamics (AAMD) simulations. **h** Vertical positions of the interaction layers compared to solvent components. The data on the left was obtained from AAMD simulations, with a simulation snapshot shown on the right. **i** Dimerization domains separated by the intermediate positions. **j** Dimerization pathway of TMHC2 observed using our single-molecule tweezers.

and the distances to the transition states ($\Delta x^{\dagger}$) (Fig. 7a and Supplementary Fig. 22). By further correcting for ELP linker length—via extrapolation to the minimum monomer distance (Supplementary Fig. 23)—we estimated the post-diffusion transition kinetics at zero force ($k_{0,m}$, $\Delta x^{\dagger}_m$) (Fig. 7b).

The initial $D_{TM\text{-}edge}$ association ($M \rightarrow I_1$) is rate-limiting ($k_{a0,m} = 7.5\ s^{-1}$), likely reflecting the slow initiation of monomer binding (Fig. 7c). Subsequent associations occur more rapidly, with $k_{a0,m} = 36.9\ s^{-1}$ for the $D_{TM\text{-}core}$ domain ($I_1 \rightarrow I_2$) and $k_{a0,m} = 15.0\ s^{-1}$ for the $D_{soluble}$ domain ($I_2 \rightarrow D$). In contrast, dissociations are much slower

https://doi.org/10.1038/s41467-025-62852-1

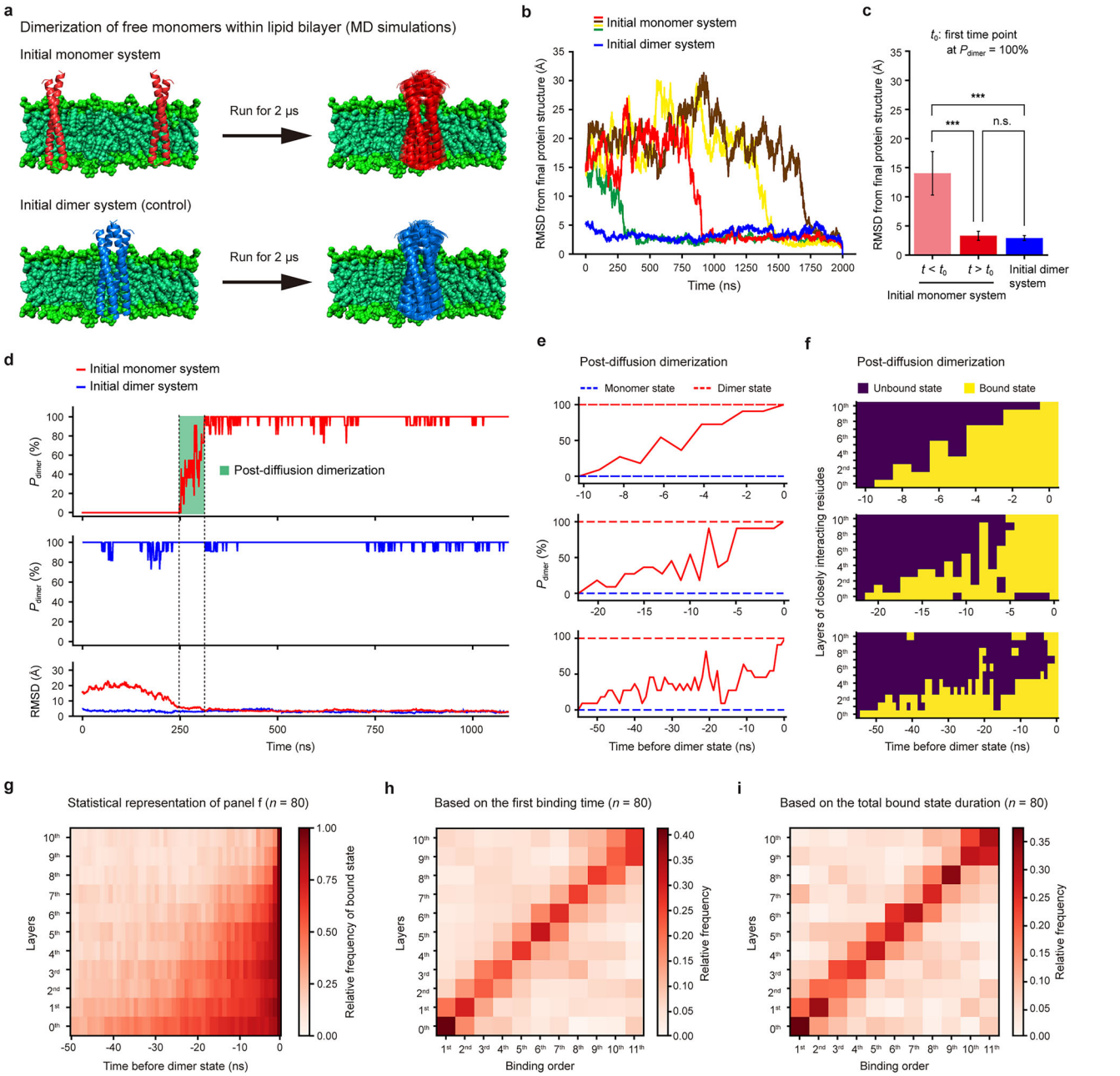

Fig. 6 | Predominant dimerization pathway under force-free conditions. **a** Coarse-grained molecular dynamics (CGMD) simulations to identify the predominant dimerization pathway of TMHC2. **b** Root mean square deviation (RMSD) from the final protein structure at 2 μs. **c** Average RMSD for the initial monomer system ($n = 80$ simulations; mean ± SD) and the initial dimer systems ($n = 5$ simulations; mean ± SD). One-way ANOVA with post-hoc Tukey HSD test shows $p < 1.0 \times 10^{-10}$ between monomer systems before and after t_0, $p < 1.0 \times 10^{-10}$ between monomer ($t < t_0$) and dimer systems, and $p = 0.951$ between monomer ($t > t_0$) and dimer systems. Statistical significance is indicated as *** for $p < 0.001$ and n.s. for $p > 0.05$. P_{dimer} indicates the percentage of dimerization. **d** Percentage of dimerization (P_{dimer}) as a function of time. Representative P_{dimer} traces are shown for both the initial monomer and dimer systems, with RMSD shown at the bottom for comparison. **e** Percentage of dimerization (P_{dimer}) during the post-diffusion dimerization period (green-boxed region in (**d**)). Three representative traces are shown. **f** Barcode plots for binding at each interaction layer. The plots are derived from the same trajectories analyzed in (**e**). **g** Statistical representation for binding at each interaction layer during the post-diffusion dimerization period ($n = 80$ simulations). Values of 0 and 1 are assigned to the unbound and bound regions in (**f**), respectively, and then averaged across 80 trajectories. **h**, **i** Binding order across the interaction layers ($n = 80$ simulations). The binding order is analyzed using two different criteria: the first binding time and the total bound state duration during the post-diffusion dimerization period.

than associations across all domains ($k_{d0,m}$'s < 1 s^{-1}), indicating high kinetic stability. Among these, the $D_{TM\text{-}core}$ domain dissociates particularly slowly ($k_{d0,m} = 0.03\ s^{-1}$), approximately 16–27 times slower than other domains, making it the rate-limiting step in dissociation. Notably, complete dimer dissociation ($D \rightarrow M$) is ~10^3 times slower than $D_{TM\text{-}core}$ dissociation alone (Supplementary Fig. 9). This high overall kinetic stability likely arises from rapid re-association events that occur before full dissociation—particularly for the $D_{TM\text{-}core}$ domain, which re-associates ~10^3 times faster than it dissociates (Fig. 7c).

Based on the kinetic estimates and intermediate positions, we reconstructed the free energy landscape for the post-diffusion dimerization (Fig. 7d and Supplementary Fig. 24). The post-diffusion rate constants ($k_{0,m}$'s) were converted into energy barrier heights ($\Delta G^{\dagger}_m$'s) using the Kramers rate framework[76]: $k_{0,m} = k_\omega \cdot \exp(-\Delta G^{\dagger}_m /$

https://doi.org/10.1038/s41467-025-62852-1

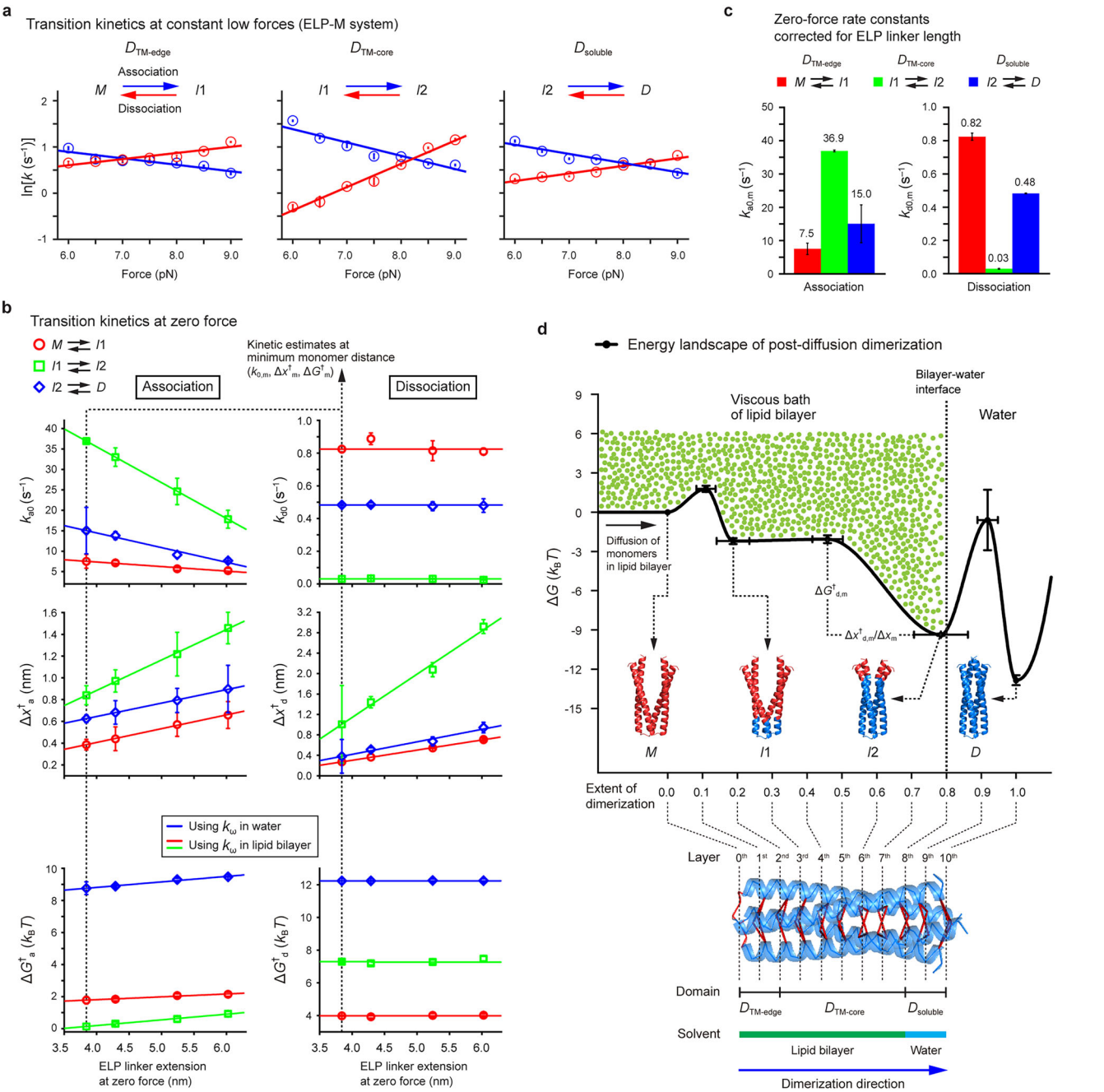

Fig. 7 | Post-diffusion kinetics and energy landscape in TM protein dimerization. a Rate constants (k) for transitions in TMHC2 as a function of force. The data correspond to those in the ELP-M linker system, with association and dissociation indicated in blue and red, respectively. The symbols M, I_1, I_2, and D indicate the monomer, intermediate 1, intermediate 2, and dimer states, respectively. The data presented as mean ± SE. Supplementary Table 1 provides details on the number of data points and molecules used for these data. **b** Transition kinetics at zero force as a function of ELP linker extension. The zero-force kinetics (k_0 and $\Delta x^\dagger$) are obtained from extrapolation analysis of the data in **a**, where k_0 and $\Delta x^\dagger$ are the rate constant at zero force and the distance to the transition state, respectively. The energy barrier height ($\Delta G^\dagger$) is derived from k_0 using the Kramers rate framework, with different values of the frequency factor (k_ω) depending on whether the transitions occur in water or lipid bilayers. The data in this panel are extrapolated to the minimum distance between monomers to obtain the zero-force transition kinetics with ELP linker length corrected ($k_{0,m}$, $\Delta x^\dagger_m$, and $\Delta G^\dagger_m$). The data are presented as mean ± SE. Supplementary Tables 1, 2 provide details on the number of data points and molecules used for these data. **c** Zero-force rate constant corrected for ELP linker length ($k_{0,m}$). The data are presented as mean ± SE. Supplementary Tables 1, 2 provide details on the number of data points and molecules used for these data. **d** Reconstructed free energy landscape (ΔG) of post-diffusion TMHC2 dimerization. The reaction coordinate represents the extent of dimerization from the 0th to 10th interaction layer. The green dots illustrate the high viscosity of the lipid bilayer. The bilayer-water interface is denoted by a vertical dashed line. The TMHC2 dimer structure and designated interaction layers shown at the bottom serve as the structural reference for the extent of dimerization. The regions of dimerization domains and corresponding solvents are indicated below the protein structure. The symbols $D_{TM\text{-}edge}$, $D_{TM\text{-}core}$, and $D_{soluble}$ represent the respective dimerization domains: the edge transmembrane (TM) domain, core TM domain, and soluble domain. The blue arrow indicates the direction of dimerization from the M to D state. The data are presented as mean ± SE. Supplementary Tables 1, 2 provide details on the number of data points and molecules used for this energy landscape reconstruction.

k_BT), where k_ω is the frequency factor. Distinct k_ω values were applied to account for differences in solvent viscosity[63,77]—$k_\omega = 10^4$–10^6 s^{-1} for soluble domains in water[78] and k_ω = ~45 s^{-1} for TM domains in lipid bilayers[63]. Transition state positions were estimated from the corresponding $\Delta x^{\dagger}_m$ values (Methods).

The initial $D_{TM\text{-}edge}$ association ($M \rightarrow I_1$) requires minimal energy ($\Delta G^{\dagger}_{a,m} = 1.8\ k_BT$), slightly exceeding the thermal fluctuation energy of ~1 k_BT (Fig. 7d). The subsequent $D_{TM\text{-}core}$ association ($I_1 \rightarrow I_2$) proceeds nearly 'downhill', with an energy barrier of only 0.1 k_BT. Once formed, however, this association contributes significantly to the dimer's thermodynamic stability ($\Delta G_{m,TM\text{-}core} = 7.2\ k_BT$ *vs* $\Delta G_{m,others} = 2.3$–$3.5\ k_BT$). The final $D_{soluble}$ association ($I_2 \rightarrow D$) requires a large energy input of 8.8 k_BT, completing the dimerization process. Once fully assembled, the dimer exhibits high kinetic and thermodynamic stability ($\Delta G^{\dagger}_{d,m,D\text{-}I2} = 12.2\ k_BT$ and $\Delta G_{m,D\text{-}M} = 12.8\ k_BT$). Notably, the first dissociation barrier ($\Delta G^{\dagger}_{d,m,D\text{-}I2}$) is the highest and lies closest to the dimer state, underscoring its structural rigidity.

Ostensibly, the barrier height estimates contradict the rate constant estimates—while the $D_{TM\text{-}core}$ domain is rate-limiting in dissociation (Fig. 7c), the $D_{soluble}$ domain is energetically limiting, exhibiting the highest dissociation barrier (Fig. 7d). However, this apparent mismatch simply arises from differences in solvent viscosity between water and lipid bilayers, as reflected in the frequency factor (k_ω). The high viscosity of lipid bilayers slows molecular transitions substantially —by a factor of ~10^2–10^4 compared to water[63,77]—thereby making a TM domain rate-limiting in dissociation. A similar pattern is observed in association: the $D_{TM\text{-}edge}$ domain is rate-limiting in association (Fig. 7c), whereas the $D_{soluble}$ domain is energetically limiting, with the highest association barrier (Fig. 7d). The large energy barrier for $D_{soluble}$ association likely arises in part from rapid molecular motions in water, which hinder the formation of stable native residue contacts. Conversely, its high dissociation barrier partially reflects strong native interactions, including electrostatic forces, hydrogen bonding, and van der Waals contacts (Fig. 5g).

Profiling peptide-mediated modulation of TM protein dimerization

Drug molecules primarily act on the post-diffusion dimerization events via intermolecular interactions. We therefore evaluated our method's sensitivity in detecting drug-induced perturbations using short peptides (Fig. 8a and Supplementary Fig. 4c). Specifically, we used a 7-aa peptide (peptide I) targeting the 9th–10th interaction layers to selectively engage the $D_{soluble}$ domain, and a 13-aa peptide (peptide II) targeting the 7th–10th layers, slightly extending into the $D_{TM\text{-}core}$ domain and covering only ~23% of it. These peptides are expected to modulate downstream transitions without fully blocking inhibition, thereby inducing localized effects (Fig. 8a).

In the force-ramp experiments with 10 μM peptide (Fig. 8b), peptide I caused only a slight reduction in the probability of complete dimerization (92%), whereas peptide II led to a substantial decrease (38%) (Fig. 8c and Methods). For peptide II, the remaining 62% of traces exhibited partial dimerization, characterized by aberrant dissociation patterns with either small or undetectable step sizes (Fig. 8d and Supplementary Fig. 25). As expected, intermediate concentrations of peptide II resulted in moderate inhibitory effects compared to the 10 μM condition (Fig. 8c). Specifically, the probability of complete dimerization decreased to 79% at 0.1 μM and 51% at 1 μM, confirming the concentration-dependent nature of peptide-mediated inhibition.

We further performed detailed profiling of peptide II-mediated effects on the intermediate states, transition kinetics, and free energy landscape using the force-clamp experiments (Fig. 8e–j, Supplementary Figs. 14, 16, 26, and Supplementary Table 2). We selected the 10 μM peptide concentration as a representative condition for detailed analysis. While peptide II did not alter the positions of the intermediate states (Fig. 8e, f and Supplementary Fig. 18), it significantly increased the population of the partially dimerized I_1 state by 41% (Fig. 8g and Supplementary Fig. 17). These results suggest that peptide II primarily traps the dimerization process at the I_1 intermediate, which corresponds to the initial $D_{TM\text{-}edge}$ association. Moreover, although the transition kinetics of the $D_{TM\text{-}edge}$ domain remained largely unaffected (Fig. 8h and Supplementary Fig. 22), peptide II delayed the subsequent associations of the $D_{TM\text{-}core}$ and $D_{soluble}$ domains by ~2-fold and similarly facilitated the dissociation of the $D_{soluble}$ domain. Notably, it accelerated the dissociation of the $D_{TM\text{-}core}$ domain by ~25-fold (Fig. 8h), indicating that peptide II more selectively destabilizes the $D_{TM\text{-}core}$ domain by markedly increasing its dissociation rate.

Similarly, peptide II reshaped the dimerization energy landscape, with its primary effect localized to the $D_{TM\text{-}core}$ domain (Fig. 8i). While it had almost no impact on the I_1 state ($\Delta\Delta G_{M\text{-}I1} = -0.2\ k_BT$), it largely destabilized the I_2 state ($\Delta\Delta G_{I1\text{-}I2} = +4.0\ k_BT$) by lowering the dissociation barrier of the $D_{TM\text{-}core}$ domain by 3.4 k_BT. Additionally, the peptide shifted the transition state position of the $D_{TM\text{-}core}$ domain from the 4th to the 6th interaction layer (Fig. 8i). This transition state shift likely reflects the need for extended association up to the 6th layer to overcome peptide binding at the 7th–10th layers (Fig. 8i, inset). The energy profile of the final $D_{soluble}$ domain also shifted upward, but its overall shape remained largely unchanged—suggesting that the shift is merely due to a propagated perturbation from the $D_{TM\text{-}core}$ domain. Together, these findings indicate that peptide II selectively perturbs the $D_{TM\text{-}core}$ domain in both kinetic and thermodynamic dimensions (Fig. 8i, j). Remarkably, despite targeting only 23% of the domain, peptide II strongly inhibited complete dimerization.

Assessing the effects of mutations at the dimerization interface

Based on our kinetic and energetic analyses, as well as the peptide inhibition results, the $D_{TM\text{-}core}$ domain appears to be the primary contributor to both the kinetic and thermodynamic stability of the TM dimer (Fig. 7c, d and Fig. 8h, i). To further investigate how specific residue mutations within the $D_{TM\text{-}core}$ domain affect overall dimer stability, we performed site-directed, alanine-scanning-type mutagenesis at the dimerization interface. Given the relatively low throughput of our current single-molecule setup, we focused on three representative mutation sites spanning the upstream, middle, and downstream regions of the $D_{TM\text{-}core}$ dimerization interface—I51A at the 3rd layer, I58A at the 5th layer, and Q65A at the 7th layer (Fig. 9a)—and analyzed their effects using the force-ramp experiments (Fig. 9b).

While the 3rd-layer I51A mutant showed a comparable proportion of successful dimerization events relative to the wild-type construct, mutations at the 5th and 7th layers led to marked reductions in dimerization success rates, regardless of whether the interactions were native or non-native (Fig. 9c). Notably, the 7th-layer Q65A mutation caused a noticeable drop in the dimerization success rate—from 99% to 36%—indicating a strong disruption of native dimer formation. This result is consistent with the peptide inhibition data, in which peptide II—targeting residues from the 7th to 10th layers—strongly suppressed complete dimerization (Fig. 8c). Regarding dimer stability, the 3rd-layer I51A mutant exhibited a modest stabilizing effect, as reflected by a slight increase in the most probable dissociation force (F^*) from 25.7 pN to 29.3 pN (Fig. 9d). In contrast, both the 5th-layer I58A and 7th-layer Q65A mutations dramatically reduced F^* to 7.0 pN and 12.4 pN, respectively, indicating significant destabilization of the dimer (Fig. 9d).

Interestingly, the dissociation forces and step sizes of the 5th- and 7th-layer mutants deviated from the WLC model predictions far more than those of the wild-type or the 3rd-layer mutant (Fig. 9e, f). While moderate deviations are expected due to stochastic molecular dissociation under thermal fluctuations, the extent of deviation—quantified as the normalized minimum distance to the WLC line (Fig. 9f, inset; see caption for details)—was approximately 2–3 times greater for these destabilizing mutants and was accompanied by markedly higher

https://doi.org/10.1038/s41467-025-62852-1

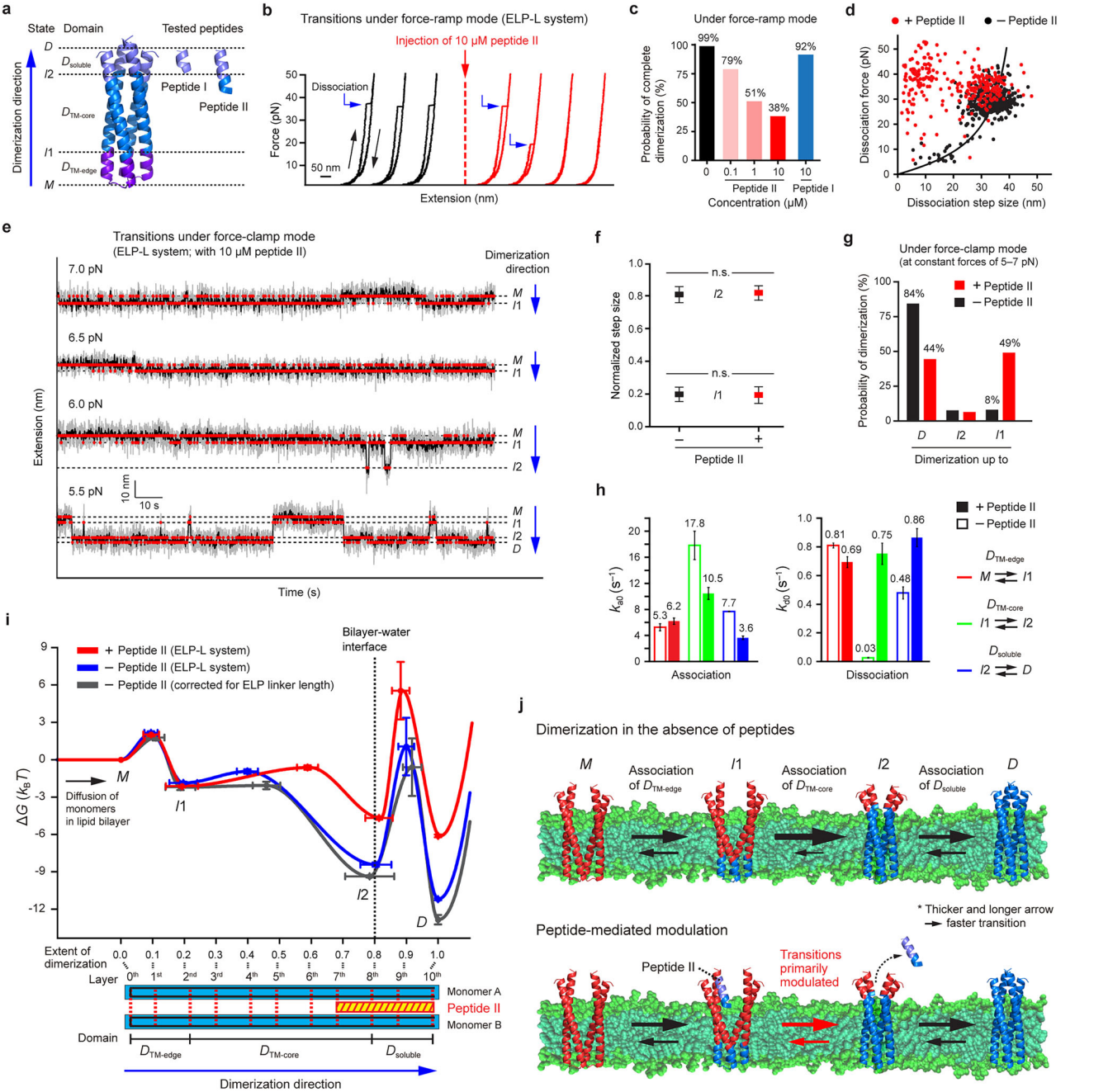

Fig. 8 | Peptide-mediated modulation of TM protein dimerization. a TMHC2 dimer and tested peptides (peptide I and II). The symbols $D_{soluble}$, $D_{TM\text{-}core}$, and $D_{TM\text{-}edge}$ represent the respective dimerization domains: the soluble domain, core transmembrane (TM) domain, and edge TM domain. The domain regions targeted by the peptides are illustrated in different colors. The symbols D, I_2, I_1, and M indicate the dimer, intermediate 2, intermediate 1, and monomer states, respectively. **b** Force-extension curves of a single TMHC2 before and after the injection of 10 μM peptide II. **c** Probability of complete dimerization before and after peptide injection in the force-ramp experiments (n = 432–543 traces from 5–7 molecules). **d** Scatter plots of dissociation forces and step sizes in the presence or absence of 10 μM peptide II (n = 432–500 data points from 5–7 molecules). The data are analyzed using the worm-like chain model (curved line). **e** Time-resolved extension traces of a single TMHC2 in the presence of 10 μM peptide II. The gray, black, and red traces represent raw traces, median-filtered traces, and traces identified using a hidden Markov model, respectively. **f** Normalized step sizes for the intermediates at 5–7 pN in the presence or absence of 10 μM peptide II (mean ± SD; n = 107 data points from 12 molecules in the presence of peptide; n = 142 data points from 13 molecules in the absence of peptide). One-way ANOVA with post-hoc Tukey HSD test (n.s. for $p > 0.05$). **g** Probability of dimerization up to each state in the force-clamp experiments (with or without 10 μM peptide II; n = 224–342 traces from 12–13 molecules). **h** Zero-force rate constants (k_0) in the presence or absence of 10 μM peptide II under the ELP-L linker system. The data are presented as mean ± SE. Supplementary Tables 1, 2 provide details on the number of data points and molecules used for these data. **i** Reconstructed free energy landscape (ΔG) of TMHC2 dimerization in the presence or absence of 10 μM peptide II. The reaction coordinate represents the extent of dimerization from the 0th to 10th layer. The TMHC2 dimer structure is shown at the bottom, with the interaction layers and the binding position of peptide II indicated. The data are presented as mean ± SE. Supplementary Tables 1, 2 provide details on the number of data points and molecules used for this energy landscape reconstruction. **j** Peptide-mediated modulation of TMHC2 dimerization at the level of dimerization domains. Thicker and longer arrows represent faster transitions.

https://doi.org/10.1038/s41467-025-62852-1

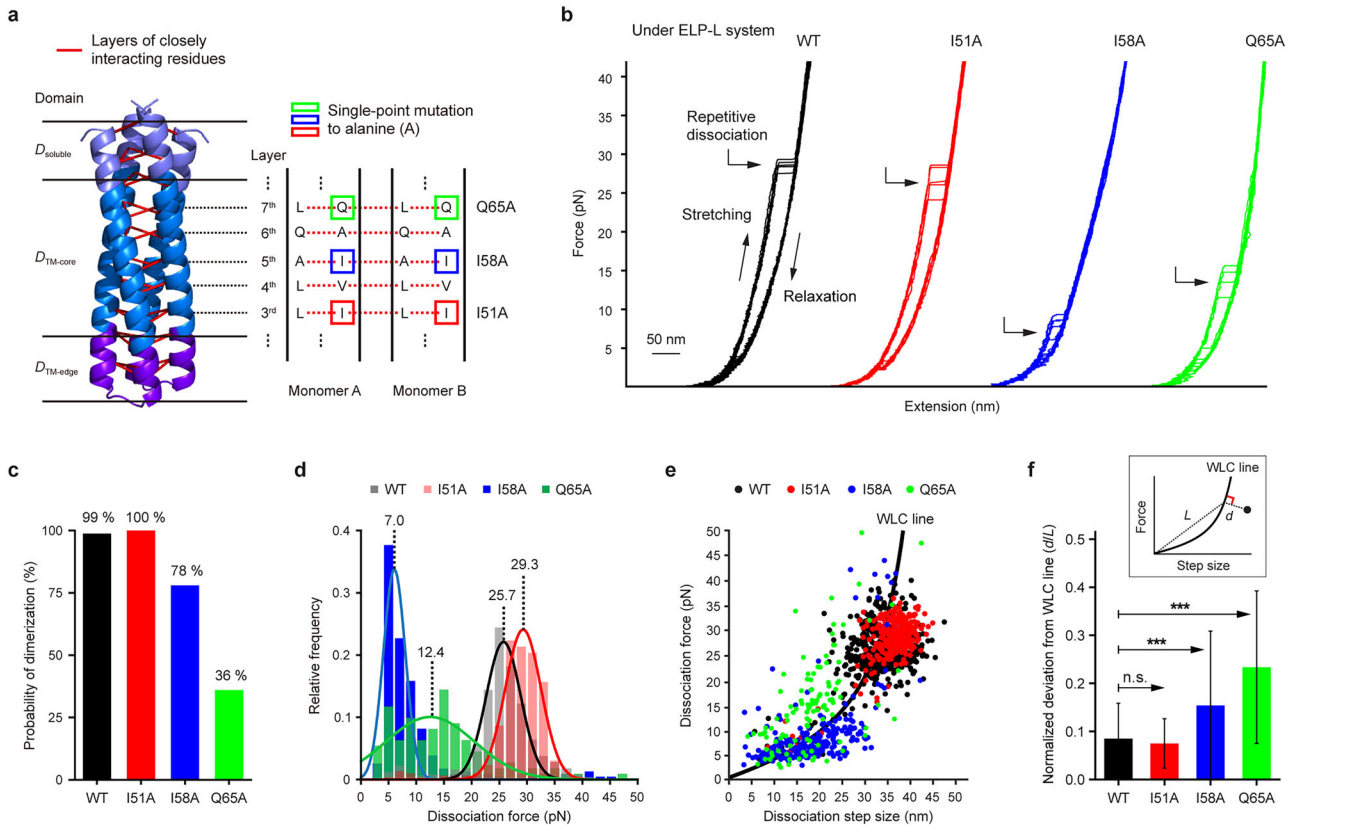

Fig. 9 | Effects of mutations at the dimerization interface. a TMHC2 dimer structure highlighting alanine mutation sites. **b** Force-extension curves for the wild-type (WT) and each mutant acquired during force-ramp experiments using the ELP-L linker system. **c** Dimerization probabilities for WT and each mutant in the force-ramp experiments (WT: $n = 500$ traces from 5 molecules; mutants: $n = 300$ traces from 3 molecules each). **d** Distributions of dissociation forces for WT and each mutant in the force-ramp experiments (WT, I51A, I58A, and Q65A: $n = 494$, 300, 234, and 111 data points from 5, 3, 3, and 3 molecules, respectively). **e** Scatter plots of dissociation forces and step sizes for WT and each mutant (same n values as in **d**). The data are analyzed using the worm-like chain (WLC) model. **f** Normalized deviation from the WLC model (d/L) for WT and each mutant (same n values as in **d**). Since the extent of deviation increases with the magnitude of the data, each data point's minimum distance to the WLC line (d) is normalized by the distance from the origin to its projection onto the WLC line (L). The inset illustrates the distance parameters d and L. One-way ANOVA with post-hoc Tukey HSD test shows no significant difference between WT and I51A ($p = 0.544$), while deviations from WLC model are significantly higher for I58A ($p < 1.0 \times 10^{-10}$) and Q65A ($p = 9.89 \times 10^{-9}$) compared to WT. Statistical significance is indicated as *** for $p < 0.001$ and n.s. for $p > 0.05$. The data are presented as mean ± SD.

variances (Fig. 9f, main panel). These results suggest that the 5th- and 7th-layer mutations may compromise both local interactions and global structural integrity, leading to heterogeneous, non-native dimer populations. This effect is particularly pronounced for the Q65A mutation at the 7th layer, which showed the greatest deviation from the WLC model and the broadest distribution of dissociation forces (Fig. 9d–f). These observations align with our energy landscape mapping, which indicate that thermodynamic stabilization of the TM dimer is primarily established through interactions extending up to the 7th–8th layers (Fig. 7d).

Discussion

Various SMFS methods, based on magnetic/optical tweezers or atomic force microscopy (AFM), have been developed to investigate protein-protein interactions at the single-molecule level. However, these techniques are primarily limited to interactions involving water-soluble proteins/peptides or the soluble domains of TM proteins[47–61]. In contrast, our single-molecule tweezer approach enables high-resolution tracking of TM protein interactions within lipid bilayers, offering detailed structural and kinetic characterization.

Our method further provides a modular single-molecule platform applicable to a broad range of protein-protein interaction studies. In systems such as magnetic and optical tweezers, tethering target molecules with linkers is essential to prevent permanent dissociation and enable repeated association cycles. A common and convenient strategy involves genetically fusing the proteins of interest with a polypeptide linker[47,50,52,53,61]. However, this method often suffers from low expression yields, particularly for TM proteins, making such constructs difficult to produce. To overcome this limitation, our approach employs an ELP linker flanked by SnoopCatcher modules, which can be easily expressed and purified in large quantities. These SnoopCatchers rapidly and covalently bind to SnoopTags engineered at the termini of the target TM proteins, ensuring efficient and robust tethering.

Dimerization of TM proteins is often simplified as a two-state process, in which monomers diffuse and then transition into dimers in a single step. However, this model overlooks the complexity of post-diffusion events, as monomer diffusion alone does not dictate the specific patterns of association that follow initial contact. Understanding these residue-level interactions is critical, particularly because pharmacological agents primarily act on post-diffusion binding events rather than on the diffusion process itself.

Our single-molecule tweezer platform enables high-resolution mapping of post-diffusion transitions within lipid bilayers, providing structural, kinetic, and energetic insights into specific dimerization domains. Even when applied to a simplified TM dimer model, this approach yields several broadly applicable insights: (1) dimerization domains are primarily defined by changes in specific residue interactions rather than by bilayer-water interfaces alone; (2) TM domains

tend to be rate-limiting in dimerization due to the high viscosity of lipid bilayers, which substantially slows molecular transitions; (3) water-soluble domains are more likely to be energetically limiting, owing to rapid molecular motions in aqueous environments that hinder the formation of stable native interactions; (4) the kinetic and energetic contributions of dimerization domains can be distinct and locally variable, presenting opportunities for precise modulation of dimerization using molecular agents.

Our method can be extended to study more complex TM protein dimerization and interaction systems of biological and pharmaceutical relevance. For example, our platform may uncover previously inaccessible dynamics of ligand-induced dimerization in cancer-associated EGFR family proteins. With growing interest in designed peptides as therapeutic agents for inhibiting TM dimerization[1,12,14,15,21–25], our approach also enables the detection of subtle, peptide-mediated modulation at the level of dimerization domains. For instance, based on our peptide-inhibition results, a tested peptide comprising a soluble segment and a minimal TM portion appears to act in a modular fashion—i.e., the soluble segment anchors to the target's soluble domain, while the TM segment perturbs both the kinetic and thermodynamic stability of the target's TM domain, effectively suppressing complete dimerization. Therefore, our single-molecule tweezer platform provides a powerful tool for dissecting the mechanisms of action of TM dimer-targeting drugs at single-molecule resolution.

Methods

Protein expression and purification

The monomeric construct of the designed transmembrane (TM) homodimer TMHC2[62] studied in this work contains SpyTag and SnoopTag sequences at its N-terminus[79,80], linked by GGSGGS linkers (Supplementary Fig. 1). These peptide tags enable the attachment of DNA handles via SpyTag-SpyCatcher binding[63,79,81], and the attachment of elastin-like polypeptide (ELP) linkers via SnoopTag-SnoopCatcher binding[59,80] (Supplementary Fig. 3). For the ELP linker constructs, the ELP sequences of three different lengths were inserted between two SnoopCatcher sequences (Supplementary Fig. 1). To prevent unwanted unfolding of the C-terminal SnoopCatcher, cysteine residues were introduced at the start and end positions of its sequence, enabling the spontaneous formation of disulfide bond knots (Supplementary Figs. 2, 3). The corresponding gene blocks were cloned into the pET24a vector using NdeI/NotI restriction sites. The assembled plasmids were transformed into *E. coli* BL21(DE3) cells (Thermo Fisher, EC0114) through heat shock transformation for 40 s at 42 °C. For TMHC2, cells were cultured in 1 L of Luria Broth (LB) medium with 25 μg/mL kanamycin at 37 °C until an OD_{600} of 0.8. For the ELP linker constructs, cells were cultured in 1 L of Terrific Broth (TB) medium with 25 μg/mL kanamycin at 37 °C until an OD_{600} of 1.0. Protein overexpression was induced by adding 200 μM IPTG (for TMHC2) or 400 μM IPTG (for the ELP linker constructs), and incubated for 3 hr at 37 °C. The cells were pelleted by centrifugation (5993 × *g*, 10 min, 4 °C) and resuspended in a lysis buffer: for TMHC2, 25 mM Tris-HCl, pH 7.4, 150 mM NaCl, 10% glycerol, 1 mM PMSF, 0.8 μg/ml pepstatin A, 0.8 μg/ml leupeptin, and 4 μg/ml aprotinin; for the ELP linker constructs, 50 mM Tris-HCl, pH 7.4, 200 mM NaCl, 1 mM TCEP, 10% glycerol, and 1 mM PMSF. Cell lysis was conducted using Emulsiflex-C3 at ~17,000 psi. For TMHC2, an additional step was added to extract membrane proteins—1% DDM detergent (GoldBio, DDM50) was added to the lysate, and the sample was incubated for 1 hr at 4 °C. Cell debris was removed by centrifugation (34,811×*g*, 30 min, 4 °C), and the supernatant was incubated with 1 ml Ni-IDA resin (Clontech, 635662) for 1 hr at 4 °C. The resin was packed into a column and washed with a wash buffer: for TMHC2, 25 mM Tris-HCl, pH 7.4, 150 mM NaCl, 10% glycerol, 0.1% DDM, and 20 mM imidazole; for the ELP linker constructs, 50 mM Tris-HCl, pH 7.4, 200 mM NaCl, 10% glycerol, and 20 mM imidazole. The protein was eluted with an elution buffer: for TMHC2, 25 mM Tris-HCl, pH 7.4, 150 mM NaCl, 10% glycerol, 0.1% DDM, and 300 mM imidazole; for the ELP linker constructs, 50 mM Tris-HCl, pH 7.4, 200 mM NaCl, 10% glycerol, and 300 mM imidazole. For TMHC2, further purification was performed using gel filtration (Cytiva, Superdex 200 10/30) in 25 mM Tris-HCl, pH 7.4, 150 mM NaCl, and 0.1% DDM. The purified samples were concentrated to ~10 μM (for TMHC2) or ~100 μM (for the ELP linker constructs) using Amicon Ultra-4 Centrifugal Filter Unit (3 kDa or 10 kDa, respectively; Merck), and then stored in aliquots at −80 °C (Supplementary Fig. 2). For the Cys mutant of TMHC2, the same procedure as for TMHC2 was followed, except that the growth medium was switched to TB. Other proteins used in this work, such as mSpyCatcher and traptavidin, were also purified following formerly developed procedures[63,71] (Supplementary Fig. 1).

Molecular construct preparation for single-molecule tweezer experiments

2 μl of each ~100 μM ELP linker construct was mixed with 10 μl of ~10 μM TMHC2 and incubated for 3 hr at 25 °C to form the TMHC2-ELP complex through SnoopTag-SnoopCatcher binding, with a covalent isopeptide bond forming spontaneously[80]. Two types of 1022-bp DNA handles were then attached to the TMHC2-ELP complex described below[63,70,71]. The DNA constructs, modified at one end with primary amine and at the other end with either azide or dual biotins (2×biotin), were generated using polymerase chain reaction (PCR) with λ DNA template (NEB, N3011S) and synthesized primers (IDT). The primers used in the PCR were a forward primer (ACAGAAAGCCGCAGAGCA) modified with amine at the 5′ end and a reverse primer (TCGCCACCATCATTTCCA) modified with azide or 2×biotin at the 5′ end. ~8 ml of the PCR product (azide-DNA:2×biotin-DNA = 1:1) was purified using HiSpeed Plasmid Maxi Kit (Qiagen, 12663) and eluted with 1 ml of 0.1 M sodium bicarbonate, pH 8.3. For maleimide modification at the amine end of DNA using amine-NHS ester reaction, ~1 μM of the eluted DNA sample was mixed with 4 μl of 250 mM $SM(PEG)_2$ (Thermo Scientific Pierce, 22102) and incubated for 20 min at ~23 °C. The sample was purified using Econo-Pac 10DG Desalting Column (Bio-Rad) and eluted with 1.5 ml of 0.1 M sodium phosphate, pH 7.3, 150 mM NaCl. To conjugate mSpyCatcher (with a cysteine) to the maleimide-modified DNA, ~0.5 μM of the eluted DNA sample was mixed with 200 μl of ~100 μM mSpyCatcher and incubated for 2 hr at ~23 °C. Free proteins were removed using HiTrap Q HP column (Cytiva, 17115401) with gradient elution from 0 to 1 M NaCl in 20 mM Tris-HCl (pH 7.5). The DNA peak fractions (~30% of which corresponded to mSpyCatcher-conjugated DNA) were concentrated to ~100 nM for the conjugated construct and stored at −80 °C in 10 μl aliquots. The mSpyCatcher-conjugated DNA handles were then attached to the N-terminal ends of the monomers in the TMHC2-ELP complex through SpyTag-SpyCatcher binding, with a covalent isopeptide bond forming spontaneously[79]. To this end, 3 μl of the TMHC2-ELP complex sample was mixed with 10 μl of the mSpyCatcher-DNA sample and incubated for 2 hr at 25 °C, yielding the final target construct (DNA-TMHC2-ELP complex; Supplementary Figs. 2, 3). The mixture was diluted to ~200 pM for the final target construct, with azide at one end and 2×biotin at the other end, and stored at −80 °C in 10 μl aliquots. The dilution buffer was 25 mM Tris-HCl, pH 7.4, 150 mM NaCl, and 1.5% bicelle. The bicelles were composed of DMPC lipids (Avanti, 850345 P) and CHAPSO detergents (Merck, C3649) at a 2.5:1 molar ratio[63,71].

Sample chamber preparation for single-molecule tweezer experiments

The coverslips (VWR, No. 1.5, 24 × 50 mm and 24 × 40 mm) were cleaned using KOH and Piranha solution[63,71]. The bottom coverslip (24×50 mm) was passivated with a polyethylene glycol (PEG) mixture of methyl-PEG (Laysan Bio, MPEG-SVA-5000) and biotin-PEG (Laysan Bio, Biotin-PEG-SVA-5000) at a 100:1 molar ratio[63,71]. These two surface-treated coverslips were assembled to construct a single-molecule

sample chamber with a channel volume (CV) of ~10 μl (1 CV). 1 μl of streptavidin-coated polystyrene beads (Spherotech, SVP-10-5) was washed and resuspended with 50 μl of 0.1 M sodium phosphate, pH 7.4, 150 mM NaCl, and 0.1% Tween 20. 1 CV of the polystyrene bead slurry was injected into the sample chamber and incubated for 2–5 min at 20–22 °C to allow for surface binding. These surface-bound polystyrene beads were used to correct for thermal drift of the sample chamber. 5 CV of 100 mg/ml bovine serum albumin (BSA) was injected into the chamber and incubated for 5 min at 20–22 °C for further surface passivation. The sample chamber was washed with 5 CV of buffer A (50 mM Tris-HCl, pH 7.4, 150 mM NaCl, and 0.1% DDM). 10 μl sample containing ~200 pM of the DNA-TMHC2-ELP complex was mixed with 1 μl of 0.04 μM traptavidin and incubated for 15 min at 20–22 °C. 1 CV of this sample was injected into the chamber and incubated for 10 min at 20–22 °C. To block unoccupied biotin-binding sites, 1 CV of a 30-nt biotin-labeled oligonucleotide (10 μM in buffer A) was injected into the chamber and incubated for 5 min at 20–22 °C. The sample chamber was washed with 5 CV of buffer B (50 mM Tris-HCl, pH 7.4, 150 mM NaCl, and 0.05% DDM). Amine-coated magnetic beads (Thermo Fisher, 14307D) were modified with dibenzocyclooctyne (DBCO; Merck, 762040) using amine-NHS ester crosslinking chemistry[63,71]. 1 μl of the DBCO-coated magnetic beads was washed and resuspended in 20 μl buffer B. 1 CV of the magnetic bead slurry was injected into the chamber and incubated for 1 hr at 25 °C. The magnetic beads were covalently attached to surface-tethered target constructs (DNA-TMHC2-ELP complex) via DBCO-azide conjugation[63,71]. The sample chamber was washed with 5 CV of buffer C (50 mM Tris-HCl, pH 7.4, 150 mM NaCl, and 1.3% bicelle). The bicelles were composed of DMPC lipids (Avanti, 850345 P) and CHAPSO detergents (Merck, C3649) at a 2.5:1 molar ratio[63,71]. In the buffer exchange experiments shown in Fig. 3d and Supplementary Fig. 7, buffer C was ultimately replaced with a buffer devoid of any lipid or detergent molecules. Specifically, the sample chamber was first washed with 4 CV of buffer A, followed by 5 CV of buffer D (50 mM Tris-HCl, pH 7.4, 150 mM NaCl).

Magnetic tweezer instrumentation

Magnetic tweezers were constructed on inverted microscopes (Olympus, IX73) equipped with motorized XY stages (ASI, MS-2000FT or Prior Scientific, H117P1)[63,70,82]. Light-emitting diodes (Thorlabs, M455L4, λ = 447 nm) were used to illuminate the magnetic beads tethered to target molecular constructs. Three-dimensional positions of the tethered beads were tracked using a charge-coupled device camera (JAI, CM-040GE or CM-030GE) at a rate of 60–90 Hz. Changes in the extension (end-to-end distance) of the target molecule correspond to variations in bead height relative to the sample chamber surface, as indicated by changes in the diffraction pattern captured by the camera. Bead heights were calibrated by recording height-dependent diffraction patterns using a piezo nanopositioner (Mad City Labs, Nano-F100S), which moves the objective lens (Olympus, UPLFLN100XO2 or UPLXAPO100XO) in precise increments to adjust the bead's diffraction patterns. Real-time tracking of bead height was achieved using chi-square analysis based on this calibration data. The non-magnetic polystyrene beads immobilized on the chamber surface were also tracked to correct for thermal drift of the sample chamber. Mechanical force was applied to the target molecule using a pair of 10 × 10 × 12 mm neodymium magnets in an antiparallel configuration with a 1-mm gap. Vertical and rotational movements of the magnets were controlled using a translational motor (PI, M-126.PD1 or M-126.PD2) and a rotational motor (PI, DT-50 or DT-34). The applied force was calibrated as a function of the magnet position using an inverted pendulum model[63,82]. The magnetic tweezer setups were mounted on pneumatic optical tables (Daeil Systems, DVIO-I-1512M-300t800H) in imaging rooms maintained at 20–22 °C.

Single-molecule tweezer experiments (force-ramp mode)

In the force-ramp experiments, mechanical force was gradually applied and released on the target molecular construct, with the following parameters: a force range of 1–50 pN, a magnet speed (m_s) of 0.1 mm/s, and a 1-s pause at either 1 or 50 pN. In our magnetic tweezer setup, the force-loading rate ranges from 0.035 to 3.1 pN/s across the force span of 1–50 pN at $m_s = 0.1$ mm/s. The force-extension curves were median-filtered for extension and smoothed for force, each using a window size of 10. The distributions of dissociation forces and step sizes in each ELP linker system were analyzed using the worm-like chain (WLC) model, represented by the Marko–Siggia equation[72,83], $FL_p/k_BT = l/L_c + (1-l/L_c)^{-2}/4 - 1/4$. In this equation, F is the applied force, k_B is the Boltzmann constant, T is the absolute temperature, l is the extension of the ELP linkers, L_p is the persistence length of the ELP linkers (measured as 0.35 nm; ref. 59), and L_c is the contour length of the ELP linkers, derived by multiplying the number of bonds between residues by the average bond length of 0.36 nm (refs. 63,84), followed by a correction accounting for the size of the dimer structure. The probability of dimerization in the force-ramp experiments in Fig. 3c was estimated as the proportion of force-extension traces showing dissociation events for each molecule. The formation of native dimers is supported by the highly monodisperse distributions of dissociation forces and step sizes (Supplementary Fig. 5). If the dimers were structurally heterogeneous or partially disordered, highly broad or polydisperse distributions would be expected, as observed under peptide-binding or site-directed mutagenesis conditions (Supplementary Fig. 25 and Fig. 9d).

Single-molecule tweezer experiments (force-clamp mode)

In the force-clamp experiments, a specified force level is driven by a rapid magnet speed of $m_s = 15$ mm/s and then maintained as constant during a specified time span. Two types of force-clamp experiments were conducted: a high-force- or low-force-clamp mode focused on characterizing the intermediate states and their transition kinetics during the dissociation or dimerization process, respectively (see the following sections for details on relevant analyses). In the high-force-clamp mode, a constant 19–20 pN was applied to the molecular construct and held for up to 3 min until monomer dissociation occurred. Following dissociation, the force was reduced back to 1 pN and held for 60 s to allow re-dimerization of monomers before beginning the next cycle. In the low-force-clamp experiments, the TMHC2 dimer was first fully dissociated into its monomers at 35 pN for 20 s (Supplementary Fig. 9c). Following dissociation, the force was reduced to a constant 5–13 pN and held for 3 min to allow re-dimerization of monomers before beginning the next cycle. The probability of dimerization up to each state in the force-clamp experiments was estimated as the proportion of time-resolved extension traces showing dimerization up to each state (Figs. 5b and 8g).

Single-molecule tweezer experiments (peptide competition)

To examine the effects of peptide competition, two types of peptides, TRTEIIR (peptide I) and TRTEIIRELERSL (peptide II), were synthesized by Peptron (South Korea) (Supplementary Fig. 4c). For the single-molecule tweezer experiments, 500 μM peptide stocks in deionized water (DW) were diluted to 0.1–10 μM using 1.3% bicelle (see the previous sections for details on bicelle composition). The same force-ramp and -clamp experiments and the relevant analyses were conducted following the injection of 5 CV peptide solution into the sample chamber. The probability of complete dimerization in the force-ramp experiments in Fig. 8c was estimated as the proportion of force-extension traces showing normal dissociation forces and step sizes consistent with the WLC model (Supplementary Fig. 25).

Analysis of dimerization intermediate states

The force-clamp extension traces were median-filtered using a 5-Hz window. The distribution of extension values was modeled using the Gaussian mixture model (GMM). The Bayesian information criterion (BIC) was used to determine the optimal number of states in the traces, defined as BIC = $q\ln(n) - 2\ln(\hat{L})$, where q is the number of output parameters given by the GMM, n is the number of data points, and $\hat{L}$ is the maximized value of the likelihood function of the GMM[84–86]. The optimal number of states was determined from the BIC plot as the elbow point, where the slope of the BIC changes substantially with the number of states[84,86] (Supplementary Fig. 14). The extension position for each state was determined using the hidden Markov model (HMM), with the initial positions derived from the GMM[63,85]. The Baum-Welch algorithm, a specific form of the expectation–maximization (EM) algorithm, was used to iteratively maximize the likelihood and optimize the HMM model parameters[63,85]. The most probable state at each time point was assigned using the Viterbi algorithm, and the dwell times in one state before transitioning to another state were calculated. Using the identified extension position for each state, the step sizes for intermediate states (I_1 and I_2) during dimerization or dissociation were normalized to the total step sizes between the monomer (M) and dimer (D) states, with values of 0 and 1 assigned to the M and D states, respectively. The normalized step sizes for the I_1 and I_2 states were determined as 0.19 ± 0.05 (SD) and 0.78 ± 0.08 (SD), respectively, and were mapped onto the protein structure based on the designated 0th–10th interaction layers. The 1st–10th layers correspond to the leucine zipper-like, closely interacting inner residues, appearing every 3–4 residues, while the 0th layer corresponds to the flexible polypeptide linker residues connecting monomer helices, allowing close interactions between the monomers (Supplementary Fig. 4a, b).

Characterization of transition kinetics between states

The transition rate constants as a function of force (k_a for association, k_d for dissociation) were obtained from the mean dwell times in one state before transitioning to another state at constant 5–13 pN (Supplementary Fig. 22). The k_a and k_d values were extrapolated to the rate constants at zero force (k_{a0}, k_{d0}) using the Bell-Evans model[72,87–89]: $k = k_0 \cdot \exp(\pm F\Delta x^{\dagger}/k_BT)$ (+ for k_d and − for k_a), where F is the applied force, $\Delta x^{\dagger}$ is the distance to the transition state, k_B is the Boltzmann constant, and T is the absolute temperature. The post-diffusion kinetics at zero force were then obtained by correcting for the ELP linker length. To this end, the k_{a0} and k_{d0} values, as a function of the ELP linker extension at zero force (d_{elp}), were extrapolated to the rate constants at the minimum distance between monomers (d_{min}), denoted as $k_{a0,m}$ and $k_{d0,m}$. The d_{elp} and d_{min} values were estimated from the root mean square end-to-end distance of the WLC polymer, $d_{rmsd} = \sqrt{2L_pL_c(1 - L_p(1 - \exp(-L_c/L_p))/L_c)}$ (refs. 90–92), and the dimer's structural information (Supplementary Fig. 23). In the d_{rmsd} formula, L_p is the persistence length of the ELP linkers (measured as 0.35 nm; ref. 59), and L_c is the contour length of the ELP linkers, derived by multiplying the number of bonds between residues by the average bond length of 0.36 nm (refs. 63,84). The estimated d_{elp} and d_{min} values were $d_{elp\text{-}l}$ = 6.02 nm, $d_{elp\text{-}m}$ = 5.24 nm, $d_{elp\text{-}s}$ = 4.29 nm, and d_{min} = 3.84 nm (Supplementary Fig. 23). The $\Delta x^{\dagger}$ values as a function of d_{elp} were also extrapolated to those at d_{min}, denoted as $\Delta x^{\dagger}_m$, which were used to reconstruct the free energy landscape for the post-diffusion dimerization (see the following section). The rate constants for complete dissociation from the D to M state were also determined from both the force-clamp and force-ramp experiments. In the force-clamp experiments, the rate constants for complete dissociation ($k_{d,com}$) as a function of force were obtained from the distributions of the total durations before transitioning from the D to M state at constant 20–30 pN (Supplementary Fig. 9b–d). To obtain the rate constant for complete dissociation at zero force ($k_{d0,com}$), the $k_{d,com}$ values were extrapolated to zero force using the Bell-Evans model, as described above (Supplementary Fig. 9d, e). In the force-ramp experiments, the cumulative plots of dissociation force distributions were normalized to obtain the dissociation probabilities as a function of force (Supplementary Fig. 9a). To obtain $k_{d0,com}$, the dissociation probability profiles were fitted with an equation derived from the first-order rate equation and the Bell-Evans equation: $P_{d,com} = 1 - \exp(\int dF(-k_{d0,com} \cdot \exp(F\Delta x^{\dagger}_{d,com}/k_BT)/\dot{F}))$ (ref. 63), where $P_{d,com}$ is the probability for complete dissociation from the D to M state, F is the force, $\dot{F}$ is the force-loading rate, $k_{d0,com}$ is the rate constant for complete dissociation at zero force, and $\Delta x^{\dagger}_{d,com}$ is the distance to the transition state.

Reconstruction of dimerization energy landscapes

The free energy landscape for the post-diffusion dimerization process was reconstructed using the kinetic estimates corrected for the ELP linker length ($k_{0,m}$ and $\Delta x^{\dagger}_m$) and the characterized intermediate positions (Supplementary Fig. 24). The energy barrier heights between the states ($\Delta G^{\dagger}_{a,m}$ and $\Delta G^{\dagger}_{d,m}$) were obtained using the Kramers rate framework[76]: $k_{0,m} = k_\omega \cdot \exp(-\Delta G^{\dagger}_m/k_BT)$, where k_ω is the frequency factor, k_B is the Boltzmann constant, and T is the absolute temperature. Different estimates of k_ω were used for different dimerization domains, reflecting its dependence on solvent viscosity[63,77]—$k_\omega = 10^4$–10^6 s^{-1} for the soluble domain exposed to water[78] and $k_\omega = 45.15 \pm 3.56$ (SE) s^{-1} for the TM domains embedded in lipid bilayers[63]. The reaction coordinate was defined as the extent of dimerization from the M to D state across the designated 0th–10th interaction layers, with values of 0 and 1 assigned to the M and D states, respectively. The positions of the intermediate states and transition states were mapped onto the reaction coordinate based on the normalized dimerization step sizes and the normalized $\Delta x^{\dagger}_{a,m}$ and $\Delta x^{\dagger}_{d,m}$ values, respectively. For comparison, the dimerization energy landscape in each ELP linker system (without linker correction) was also derived from the kinetic estimates (k_0 and $\Delta x^{\dagger}$) and the intermediate positions in each system (Supplementary Fig. 24).

Transmission electron microscopy (TEM)

Negative staining TEM was utilized to visualize bicelles and measure their sizes. A solution of 1.3% (w/v) DMPC bicelles, used in the single-molecule tweezer experiments, was applied onto a formvar/carbon-coated copper grid (Ted Pella, 01754-F). After 1 min, excess sample was blotted off using a filter paper. The grid was gently rinsed with distilled water and stained with 2% ammonium molybdate tetrahydrate for 10 s. Excess staining solution was removed using a filter paper, and the grid was left to air dry for 5 min. TEM images were obtained using JEM-1400 TEM (JEOL, Japan) operating at 120 kV. The images were analyzed using ImageJ software to determine the diameter of the bicelles.

All-atom molecular dynamics (AAMD) simulation

The AAMD simulation system was constructed using CHARMM-GUI Membrane Builder[93] (Supplementary Table 3). The protein structure of the TMHC2 dimer was obtained from AlphaFold3[62,94], and the dimer was inserted into the lipid bilayer composed of 302 DMPC molecules, using coordinates optimized by the PPM 2.0 (ref. 95). The simulation system was solvated with TIP3P water molecules[96], adjusted to pH 7.0, and neutralized with ~150 mM K^+ and Cl^- ions. The final dimensions of the system were 10.1 × 10.1 × 10.5 nm, containing a total of 100,850 atoms. Periodic boundary conditions were applied to the simulation system. The MD simulations were conducted using GROMACS (version 2021.4) with CHARMM36m force field (charmm36-mar2019)[97,98]. The simulation system was energy-minimized using the steepest descent algorithm. During the energy minimization, van der Waals (vdW) interactions were calculated with a cutoff distance of 12 Å, smoothly switching off at 10–12 Å using a force-switch function[99]. Long-range electrostatic interactions were calculated using the Particle-Mesh

Ewald (PME) method with a cutoff distance of 12 Å (ref. 100). The LINCS algorithm was employed to impose constraints on the bond lengths involving hydrogen atoms[101]. Following the energy minimization, the system underwent a multi-stage equilibration process. Initially, the system equilibration was performed in the NVT ensemble for a total of 375,000 steps with a 1-fs time step. The temperature was maintained at 303.15 K using the Berendsen thermostat[102]. The equilibration continued in the NPT ensemble for an additional 750,000 steps with a 2-fs time step. The pressure was maintained at 1 bar using the Berendsen barostat with semi-isotropic pressure coupling and a compressibility of 4.5×10^{-5} bar^{-1} (ref. 102). The LINCS method was applied to handle the bond constraints throughout both the NVT and NPT equilibration steps. After the equilibration, a production run was performed for 1 µs with a 2-fs time step. During the production run, the temperature was maintained at 303.15 K using the Nosé-Hoover thermostat[103], and the pressure was maintained at 1 bar using the Parrinello-Rahman barostat with isotropic pressure coupling and a compressibility of 4.5×10^{-5} bar^{-1} (ref. 104). The 1-µs MD simulation of the TMHC2 dimer was analyzed using GROMACS modules, the Residue Interaction Network Generator (RING)[74,75], and Python.

Analysis of AAMD simulation trajectories

The analysis of solvent environments around the TMHC2 dimer, as shown in Fig. 5h, was conducted using a 1-ns time interval trajectory of a 1-µs AAMD simulation of the dimer. The center of the dimer was translated to the center of the simulation system using the GROMACS trjconv module. The simulation trajectory was analyzed using MDAnalysis library in Python[105]. The z-coordinates of atoms within a 2-nm radius cylinder centered on the dimer's center of mass were extracted at each time frame. The analyzed atoms include those of water molecules, lipid heads with glycerol backbone, lipid tails, and the closely interacting protein residues at the dimerization interface. The layers of closely interacting protein residues (the interaction layers) are shown in Supplementary Fig. 4a, b. The z-coordinates of the atoms were binned into 1 Å intervals, and the z-coordinate counts for each type of molecules and each interaction layer of the protein were normalized by their maximum counts. The distributions of z-coordinate counts for solvent components (water, lipid heads, and lipid tails) were compared with those for the protein's interaction layers (Fig. 5h). The intermolecular interactions between monomers in the dimer state, as shown in Fig. 5g, were also analyzed using the AAMD simulation trajectory. At each time frame, the interaction types and counts for residue pairs between the monomers were obtained using the residue interaction network generator (RING) (version 4.0; https://ring.biocomputingup.it; performed in July 2024)[74,75]. The distance thresholds for each type of interaction used in the RING analysis were as follows: 3.9 Å for hydrogen bonds between donor and acceptor, 2.5 Å for hydrogen bond between hydrogen and acceptor, 4.3 Å for π−hydrogen bond between donor and an aromatic ring center, 6.5 Å for π−π interactions between aromatic ring centers, 5 Å for π−cation interactions between an aromatic ring and the cation center of mass, 4 Å for ionic bonds (salt bridges), 2.5 Å for disulfide bonds, 2.8 Å for metal ion coordination between metal ion atoms and acceptor, and 0.01 for vdW interactions as the fraction of intersection between the vdW radii of two atoms. In this analysis, three types of intermolecular interactions−hydrogen bonds, ionic interactions, and vdW interactions−were detected between the monomers. For each interaction type, the interaction counts were summed for each interaction layer region over 1 µs (Supplementary Fig. 19 for the detailed analysis procedure).

Coarse-grained molecular dynamics (CGMD) simulation

Two CGMD simulation systems were prepared as follows: (1) the initial dimer system, where the TMHC2 dimer was embedded within the lipid bilayer, and (2) the initial monomer system, where the two monomers of TMHC2 were initially separated by ~10 nm within the lipid bilayer (Supplementary Table 3). To this end, AAMD simulation systems with the protein/membrane configurations were constructed using CHARMM-GUI Membrane Builder[93], and then converted into the coarse-grained (CG) representation using CHARMM-GUI Martini Maker with MARTINI 3.0 force field[106,107]. The lipid membranes consisted of 304 and 897 DPPC molecules for the initial dimer and monomer systems, respectively. The CGMD simulation systems were solvated with MARTINI polarized water molecules[108], adjusted to pH 7.0, and neutralized with ~150 mM Na^+ and Cl^- ions. The final dimensions of the systems were $10.0 \times 10.0 \times 10.2$ nm with 8679 beads for the initial dimer system and $17.0 \times 17.0 \times 12.9$ nm with 31,305 beads for the initial monomer system, respectively. Periodic boundary conditions were applied to both simulation systems. The CGMD simulations were conducted using GROMACS (version 2021.4) with MARTINI 3.0 force field[107]. The simulation systems were energy-minimized using the steepest descent algorithm, with vdW interactions calculated with a cutoff distance of 1.1 nm. Long-range electrostatic interactions were handled using the reaction-field method with a dielectric constant of 15 and a 1.1-nm cutoff[109]. Temperature coupling was controlled using the v-rescale thermostat with a time constant of 1.0 ps (ref. 110), maintaining the systems at 303.15 K. Semi-isotropic pressure coupling was applied using the Berendsen barostat with a time constant of 5.0 ps and a compressibility of 3×10^{-4} bar^{-1} (ref. 102). Following the energy minimization, the systems underwent a multi-stage equilibration process. Initially, the system was equilibrated in the NPT ensemble for 500,000 steps with a 2.0-fs time step, under the same temperature, pressure, and interaction conditions as in the energy minimization stage. As equilibration progressed, the time step was incrementally increased from 2.0 fs to 20.0 fs, resulting in a total equilibration time of 14 ns under periodic boundary conditions. After the equilibration stage, production runs were performed in the NPT ensemble for 2 µs with a 20-fs time step. The temperature was maintained at 303.15 K using v-rescale thermostat[110], while the pressure was controlled at 1 bar using the semi-isotropic Parrinello-Rahman barostat with a compressibility of 3×10^{-4} bar^{-1} (ref. 104). The 2-µs CGMD simulations were analyzed using GROMACS modules and Python.

Analysis of CGMD simulation trajectories

The dimerization percentage of TMHC2 as a function of time and the binding order across the interaction layers were analyzed from the CGMD simulation trajectories. The distance cutoff for binding at the interaction layers ($d_{cut,0}$) was initially determined from five independent trajectories of the initial dimer system, as described below. For each trajectory, the backbone bead coordinates of each layer's residues in two monomers were extracted at 1-ns intervals and averaged to obtain their center coordinates. The distance between the center coordinates in each layer (d_{mm}) was then calculated. The proportion of all layer's d_{mm} values below an arbitrary distance cutoff d_{cut} (P_{dimer}; dimerization percentage) was plotted as a function of d_{cut} (Supplementary Fig. 20). From the plot of P_{dimer} *vs* d_{cut}, the d_{cut} at $P_{dimer} = 99\%$ was selected as $d_{cut,0}$ (17.3 Å; Supplementary Fig. 20). For a hundred independent trajectories of the initial monomer system, the same $d_{cut,0}$ criterion was applied to obtain P_{dimer} as a function of time, as shown in Fig. 6d, e. Only 80 trajectories showed dimerization events within the 2-µs time span, and only these trajectories were considered for further analysis. The period of the post-diffusion dimerization was defined as the interval from the last time point at $P_{dimer} = 0\%$ to the first time point at $P_{dimer} = 100\%$. The criterion for determining the dimerized states in the initial monomer system was the first time point at $P_{dimer} = 100\%$. The time-resolved binding profiles at each interaction layer, as shown in Fig. 6f, g, were also determined based on the same distance cutoff, $d_{cut,0}$. The binding order across the layers was further estimated using two different criteria: the first binding time and the total bound state durations during the post-diffusion dimerization period (Supplementary Fig. 21). With each criterion, all possible

binding pathways across the layers were identified. The binding order across the layers was then quantified as the relative frequency of the rank order at each layer over all 80 trajectories that exhibited dimerization events.

Data availability

All data that support the findings of this study are available in the main text, Supplementary Information, and Source Data, as well as from the corresponding author upon request. Other raw data such as the MD simulation trajectory files have been deposited to figshare, which are available in [https://doi.org/10.6084/m9.figshare.28218593]. Source data are provided with this paper.

Code availability

Analysis codes are available in Code Ocean [https://doi.org/10.24433/CO.9572266.v1].

References

1. Mravic, M. et al. De novo-designed transmembrane proteins bind and regulate a cytokine receptor. *Nat. Chem. Biol.* **20**, 751–760 (2024).
2. Abouelkheir, M., Roy, T., Krzyscik, M. A., Ozdemir, E. & Hristova, K. Investigations of membrane protein interactions in cells using fluorescence microscopy. *Curr. Opin. Struct. Biol.* **86**, 102816 (2024).
3. Abraham, B. G. et al. Molecular basis of JAK2 activation in erythropoietin receptor and pathogenic JAK2 signaling. *Sci. Adv.* **10**, eadl2097 (2024).
4. Cai, K., Zhang, X. W. & Bai, X. C. Cryo-electron microscopic analysis of single-pass transmembrane receptors. *Chem. Rev.* **122**, 13952–13988 (2022).
5. Wilmes, S. et al. Mechanism of homodimeric cytokine receptor activation and dysregulation by oncogenic mutations. *Science* **367**, 643 (2020).
6. Bocharov, E. V. et al. Helix-helix interactions in membrane domains of bitopic proteins: Specificity and role of lipid environment. *Biochim. Biophys Acta-Biomembr***1859**, 561–576 (2017).
7. Marianayagam, N. J., Sunde, M. & Matthews, J. M. The power of two: protein dimerization in biology. *Trends Biochem Sci.* **29**, 618–25 (2004).
8. Bray, S. J. Notch signalling in context. *Nat. Rev. Mol. Cell Biol.* **17**, 722–735 (2016).
9. Liu, H. D. et al. Notch dimerization is required for leukemogenesis and T-cell development. *Genes Dev.* **24**, 2395–2407 (2010).
10. Gumbiner, B. M. Regulation of cadherin-mediated adhesion in morphogenesis. *Nat. Rev. Mol. Cell Biol.* **6**, 622–634 (2005).
11. Sakamoto, K., Chao, W. S., Katsube, K. & Yamaguchi, A. Distinct roles of EGF repeats for the Notch signaling system. *Exp. Cell Res* **302**, 281–91 (2005).
12. Yin, H. & Flynn, A. D. Drugging membrane protein interactions. *Annu. Rev. Biomed. Eng.* **18**, 51–76 (2016).
13. Federico, S. et al. Modulation of the innate immune response by targeting toll-like receptors: a perspective on their agonists and antagonists. *J. Med. Chem.* **63**, 13466–13513 (2020).
14. Albrecht, C. et al. Transmembrane peptides as inhibitors of protein-protein interactions: an efficient strategy to target cancer cells? *Front. Oncol.* **10**, 519 (2020).
15. Cai, X., Wang, D. X., Zhang, R. M., Chen, Y. C. & Chen, J. The transmembrane domains of GPCR dimers as targets for drug development. *Drug Discov. Today* **28**, 103419 (2023).
16. Li, L. & Li, J. Y. Dimerization of transmembrane proteins in cancer immunotherapy. *Membranes* **13**, 393 (2023).
17. Zubair, T. & Bandyopadhyay, D. Small molecule EGFR inhibitors as anti-cancer agents: discovery, mechanisms of action, and opportunities. *Int. J. Mol. Sci.* **24**, 2651 (2023).
18. Fu, Z. W., Li, S. J., Han, S. F., Shi, C. & Zhang, Y. Antibody drug conjugate: the "biological missile" for targeted cancer therapy. *Signal Transduct. Target. Ther.* **7**, 93 (2022).
19. Roskoski, R. J. r. Small molecule inhibitors targeting the EGFR/ErbB family of protein-tyrosine kinases in human cancers. *Pharmacol. Res.* **139**, 395–411 (2019).
20. Jonker, D. J. et al. Cetuximab for the treatment of colorectal cancer. *N. Engl. J. Med.* **357**, 2040–2048 (2007).
21. Yin, H. et al. Computational design of peptides that target transmembrane helices. *Science* **315**, 1817–1822 (2007).
22. Duart, G. et al. Computational design of BclxL inhibitors that target transmembrane domain interactions. *Proc. Natl Acad. Sci. USA.* **120**, e2219648120 (2023).
23. Mravic, M. et al. De novo designed transmembrane peptides activating the alpha5beta1 integrin. *Protein Eng. Des. Sel.* **31**, 181–190 (2018).
24. Bublil, E. M. et al. Interfering with the Dimerization of the ErbB receptors by Transmembrane domain-derived peptides inhibits tumorigenic growth in vitro and in vivo. *Biochemistry* **55**, 5520–5530 (2016).
25. Shandler, S. J. et al. Computational Design of a β-Peptide That Targets Transmembrane Helices. *J. Am. Chem. Soc.* **133**, 12378–12381 (2011).
26. Niederauer, C. et al. Dual-color DNA-PAINT single-particle tracking enables extended studies of membrane protein interactions. *Nat. Commun.* **14**, 4345 (2023).
27. Ernst, M., Orabi, E.A., Stockbridge, R.B., Faraldo-Gomez, J.D. & Robertson, J.L. Dimerization mechanism of an inverted-topology ion channel in membranes. *Proc. Natl Acad. Sci. USA* **120**, e2308454120 (2023).
28. Asher, W. B. et al. Single-molecule FRET imaging of GPCR dimers in living cells. *Nat. Methods* **18**, 397 (2021).
29. Duart, G., Grau, B., Mingarro, I. & Martinez-Gil, L. Methodological approaches for the analysis of transmembrane domain interactions: A systematic review. *Biochim Biophys. Acta Biomembr.* **1863**, 183712 (2021).
30. Yano, Y., Watanabe, Y. & Matsuzaki, K. Thermodynamic and kinetic stabilities of transmembrane helix bundles as revealed by single-pair FRET analysis: Effects of the number of membrane-spanning segments and cholesterol. *Biochim Biophys. Acta Biomembr.* **1863**, 183532 (2021).
31. Kim, D. H. et al. Direct visualization of single-molecule membrane protein interactions in living cells. *PLoS Biol.* **16**, e2006660 (2018).
32. Park, Y. et al. Single-Molecule Rotation for EGFR Conformational Dynamics in Live Cells. *J. Am. Chem. Soc.* **140**, 15161–15165 (2018).
33. Khadria, A. S. & Senes, A. Fluorophores, environments, and quantification techniques in the analysis of transmembrane helix interaction using FRET. *Biopolymers* **104**, 247–64 (2015).
34. Kasai, R. S. & Kusumi, A. Single-molecule imaging revealed dynamic GPCR dimerization. *Curr. Opin. Cell Biol.* **27**, 78–86 (2014).
35. Mineev, K. S. et al. NMR-based approach to measure the free energy of transmembrane helix-helix interactions. *Biochim. Biophys. Acta-Biomembr.***1838**, 164–172 (2014).
36. Ng, D. P. & Deber, C. M. Terminal residue hydrophobicity modulates transmembrane helix-helix interactions. *Biochemistry* **53**, 3747–57 (2014).
37. Li, E., Wimley, W. C. & Hristova, K. Transmembrane helix dimerization: beyond the search for sequence motifs. *Biochim Biophys. Acta* **1818**, 183–93 (2012).
38. Kasai, R. S. et al. Full characterization of GPCR monomer-dimer dynamic equilibrium by single molecule imaging. *J. Cell Biol.* **192**, 463–80 (2011).
39. Hong, H. & Bowie, J. U. Dramatic destabilization of transmembrane helix interactions by features of natural membrane environments. *J. Am. Chem. Soc.* **133**, 11389–98 (2011).

40. MacKenzie, K. R. & Fleming, K. G. Association energetics of membrane spanning alpha-helices. *Curr. Opin. Struct. Biol.* **18**, 412–9 (2008).
41. Blazhynska, M. et al. A rigorous framework for calculating protein-protein binding affinities in membranes. *J. Chem. Theory Comput.* **19**, 9077–9092 (2023).
42. Lamprakis, C. et al. Evaluating the efficiency of the Martini force field to study protein dimerization in aqueous and membrane environments. *J. Chem. Theory Comput.* **17**, 3088–3102 (2021).
43. Itaya, H. et al. All-atom molecular dynamics elucidating molecular mechanisms of single-transmembrane model peptide dimerization in a lipid bilayer. *ACS Omega* **6**, 11458–11465 (2021).
44. Domanski, J., Sansom, M. S. P., Stansfeld, P. J. & Best, R. B. Atomistic mechanism of transmembrane helix association. *PLoS Comput. Biol.* **16**, e1007919 (2020).
45. Domanski, J., Hedger, G., Best, R. B., Stansfeld, P. J. & Sansom, M. S. P. Convergence and sampling in determining free energy landscapes for membrane protein association. *J. Phys. Chem. B* **121**, 3364–3375 (2017).
46. Dunton, T. A., Goose, J. E., Gavaghan, D. J., Sansom, M. S. & Osborne, J. M. The free energy landscape of dimerization of a membrane protein, NanC. *PLoS Comput. Biol.* **10**, e1003417 (2014).
47. Bauer, M. S. et al. Single-molecule force stability of the SARS-CoV-2-ACE2 interface in variants-of-concern. *Nat. Nanotechnol.* **19**, 399–405 (2024).
48. Shrestha, P. et al. Single-molecule mechanical fingerprinting with DNA nanoswitch calipers. *Nat. Nanotechnol.* **16**, 1362–1370 (2021).
49. Kostrz, D. et al. A modular DNA scaffold to study protein-protein interactions at single-molecule resolution. *Nat. Nanotechnol.* **14**, 988 (2019).
50. Zhang, Y. et al. Multi-domain interaction mediated strength-building in human alpha-actinin dimers unveiled by direct single-molecule quantification. *Nat. Commun.* **15**, 6151 (2024).
51. van der Sleen, L., Stevens, J. A., Marrink, S. J., Poolman, B. & Tych, K. Probing the stability and interdomain interactions in the ABC transporter OpuA using single-molecule optical tweezers. *Cell Rep.* **43**, 114110 (2024).
52. Deng, Y. X. & Yan, J. Force-dependent structural changes of Filamin C rod domains regulated by Filamin C Dimer. *J. Am. Chem. Soc.* **145**, 14670–14678 (2023).
53. Bodescu, M. A., Aretz, J., Grison, M., Rief, M. & Fassler, R. Kindlin stabilizes the talin.integrin bond under mechanical load by generating an ideal bond. *Proc. Natl. Acad. Sci. USA* **120**, e2218116120 (2023).
54. Pandey, S. et al. Chirality transmission in macromolecular domains. *Nat. Commun.* **13**, 76 (2022).
55. Mickolajczyk, K. J., Olinares, P. D. B., Chait, B. T., Liu, S. & Kapoor, T. M. The MIDAS domain of AAA mechanoenzyme Mdn1 forms catch bonds with two different substrates. *Elife* **11**, e73534 (2022).
56. Yang, J. S. et al. Molecular interaction and inhibition of SARS-CoV-2 binding to the ACE2 receptor. *Nat. Commun.* **11**, 4541 (2020).
57. Ma, X. F. et al. Interactions between PHD3-Bromo of MLL1 and H3K4me3 revealed by single-molecule magnetic tweezers in a parallel DNA circuit. *Bioconjug. Chem.* **30**, 2998–3006 (2019).
58. Ott, W., Jobst, M. A., Schoeler, C., Gaub, H. E. & Nash, M. A. Single-molecule force spectroscopy on polyproteins and receptor-ligand complexes: The current toolbox. *J. Struct. Biol.* **197**, 3–12 (2017).
59. Ott, W. et al. Elastin-like polypeptide linkers for single-molecule force spectroscopy. *ACS Nano* **11**, 6346–6354 (2017).
60. Vera, A. M. & Carrion-Vazquez, M. Direct identification of protein-protein interactions by single-molecule force spectroscopy. *Angew. Chem. Int Ed. Engl.* **55**, 13970–13973 (2016).
61. Kim, J., Zhang, C. Z., Zhang, X. H. & Springer, T. A. A mechanically stabilized receptor-ligand flex-bond important in the vasculature. *Nature* **466**, 992–U123 (2010).
62. Lu, P. et al. Accurate computational design of multipass transmembrane proteins. *Science* **359**, 1042–1046 (2018).
63. Kim, S., Lee, D., Wijesinghe, W. C. B. & Min, D. Robust membrane protein tweezers reveal the folding speed limit of helical membrane proteins. *Elife* **12**, e85882 (2023).
64. Iyer, R. S. et al. Drug-resistant EGFR mutations promote lung cancer by stabilizing interfaces in ligand-free kinase-active EGFR oligomers. *Nat. Commun.* **15**, 2130 (2024).
65. Noordeen, N. A., Carafoli, F., Hohenester, E., Horton, M. A. & Leitinger, B. A transmembrane leucine zipper is required for activation of the dimeric receptor tyrosine kinase DDR1. *J. Biol. Chem.* **281**, 22744–22751 (2006).
66. Gurezka, R. & Langosch, D. In vitro selection of membrane-spanning leucine zipper protein-protein interaction motifs using POSSYCCAT. *J. Biol. Chem.* **276**, 45580–7 (2001).
67. Gurezka, R., Laage, R., Brosig, B. & Langosch, D. A heptad motif of leucine residues found in membrane proteins can drive self-assembly of artificial transmembrane segments. *J. Biol. Chem.* **274**, 9265–9270 (1999).
68. Wei, P. et al. The dimerization interface of the glycoprotein Ibβ transmembrane domain corresponds to polar residues within a leucine zipper motif. *Protein Sci.* **20**, 1814–1823 (2011).
69. Xu, L. D., Hu, T. T. & Luo, S. Z. Leucine Zipper Motif Drives the Transmembrane Domain Dimerization of E-cadherin. *Int. J. Pept. Res. Ther.***20**, 95–102 (2014).
70. Kim, S. et al. Hidden route of protein damage through oxygen-confined photooxidation. *Nat. Commun.* **15**, 10873 (2024).
71. Lee, D. & Min, D. Single-molecule tethering methods for membrane proteins. *Methods Enzymol.* **694**, 263–284 (2024).
72. Wijesinghe, W. C. B. & Min, D. Single-Molecule Force Spectroscopy of Membrane Protein Folding. *J. Mol. Biol.* **435**, 167975 (2023).
73. Min, D., Jefferson, R. E., Bowie, J. U. & Yoon, T. Y. Mapping the energy landscape for second-stage folding of a single membrane protein. *Nat. Chem. Biol.* **11**, 981–7 (2015).
74. Del Conte, A. et al. RING 4.0: faster residue interaction networks with novel interaction types across over 35,000 different chemical structures. *Nucleic Acids Res.* **52**, W306–W312 (2024).
75. Clementel, D. et al. RING 3.0: fast generation of probabilistic residue interaction networks from structural ensembles. *Nucleic Acids Res.* **50**, W651–W656 (2022).
76. Hanggi, P., Talkner, P. & Borkovec, M. Reaction-Rate Theory – 50 Years after Kramers. *Rev. Mod. Phys.* **62**, 251–341 (1990).
77. Min, D. Y. Folding speeds of helical membrane proteins. *Biochem. Soc. Trans.* **52**, 491–501 (2024).
78. Kubelka, J., Hofrichter, J. & Eaton, W. A. The protein folding 'speed limit'. *Curr. Opin. Struct. Biol.* **14**, 76–88 (2004).
79. Zakeri, B. et al. Peptide tag forming a rapid covalent bond to a protein, through engineering a bacterial adhesin. *Proc. Natl. Acad. Sci. USA* **109**, E690–E697 (2012).
80. Veggiani, G. et al. Programmable polyproteams built using twin peptide superglues. *Proc. Natl. Acad. Sci. USA* **113**, 1202–1207 (2016).
81. Min, D., Arbing, M. A., Jefferson, R. E. & Bowie, J. U. A simple DNA handle attachment method for single molecule mechanical manipulation experiments. *Protein Sci.* **25**, 1535–1544 (2016).
82. Kim, S. & Min, D. Robust magnetic tweezers for membrane protein folding studies. *Methods Enzymol.* **694**, 285–301 (2024).
83. Marko, J. F. & Siggia, E. D. Stretching DNA. *Macromolecules* **28**, 8759–8770 (1995).

84. Choi, H. K. et al. Watching helical membrane proteins fold reveals a common N-to-C-terminal folding pathway. *Science* **366**, 1150 (2019).
85. Zhang, Y., Jiao, J. & Rebane, A. A. Hidden Markov modeling with detailed balance and its application to single protein folding. *Biophys. J.* **111**, 2110–2124 (2016).
86. Lee, T. H. Extracting kinetics information from single-molecule fluorescence resonance energy transfer data using hidden markov models. *J. Phys. Chem. B* **113**, 11535–42 (2009).
87. Evans, E. Probing the relation between force - Lifetime - and chemistry in single molecular bonds. *Annu. Rev. Biophys. Biomol. Struct.* **30**, 105–128 (2001).
88. Evans, E. & Ritchie, K. Dynamic strength of molecular adhesion bonds. *Biophys. J.* **72**, 1541–55 (1997).
89. Bell, G. I. Models for the specific adhesion of cells to cells. *Science* **200**, 618–27 (1978).
90. Hagerman, P. J. Flexibility of DNA. *Annu. Rev. Biophys. Biophys. Chem.* **17**, 265–286 (1988).
91. Benoit, H. & Doty, P. Light scattering from non-Gaussian chains. *J. Phys. Chem.* **57**, 958–963 (1954).
92. Doose, S., Barsch, H. & Sauer, M. Polymer properties of polythymine as revealed by translational diffusion. *Biophys. J.* **93**, 1224–1234 (2007).
93. Wu, E. L. et al. CHARMM-GUI toward realistic biological membrane simulations. *J. Comput. Chem.* **35**, 1997–2004 (2014).
94. Abramson, J. et al. Accurate structure prediction of biomolecular interactions with AlphaFold 3. *Nature* **630**, 493–500 (2024).
95. Lomize, M. A., Pogozheva, I. D., Joo, H., Mosberg, H. I. & Lomize, A. L. OPM database and PPM web server: resources for positioning of proteins in membranes. *Nucleic Acids Res.* **40**, D370–D376 (2012).
96. Jorgensen, W. L., Chandrasekhar, J., Madura, J. D., Impey, R. W. & Klein, M. L. Comparison of Simple Potential Functions for Simulating Liquid Water. *J. Chem. Phys.* **79**, 926–935 (1983).
97. Van der Spoel, D. et al. GROMACS: Fast, flexible, and free. *J. Comput. Chem.* **26**, 1701–1718 (2005).
98. Huang, J. et al. CHARMM36m: an improved force field for folded and intrinsically disordered proteins. *Nat. Methods* **14**, 71–73 (2017).
99. Steinbach, P. J. & Brooks, B. R. New spherical-cutoff methods for long-range forces in macromolecular simulation. *J. Comput. Chem.* **15**, 667–683 (1994).
100. Essmann, U. et al. A smooth particle mesh Ewald Method. *J. Chem. Phys.* **103**, 8577–8593 (1995).
101. Hess, B., Bekker, H., Berendsen, H. J. C. & Fraaije, J. G. E. M. LINCS: A linear constraint solver for molecular simulations. *J. Comput. Chem.* **18**, 1463–1472 (1997).
102. Berendsen, H. J. C., Postma, J. P. M., Vangunsteren, W. F., Dinola, A. & Haak, J. R. Molecular-dynamics with coupling to an external bath. *J. Chem. Phys.* **81**, 3684–3690 (1984).
103. Hoover, W. G. Canonical dynamics - equilibrium phase-space distributions. *Phys. Rev. A* **31**, 1695–1697 (1985).
104. Parrinello, M. & Rahman, A. Polymorphic transitions in single-crystals - a new molecular-dynamics method. *J. Appl. Phys.* **52**, 7182–7190 (1981).
105. Michaud-Agrawal, N., Denning, E. J., Woolf, T. B. & Beckstein, O. Software news and updates MDAnalysis: A toolkit for the analysis of molecular dynamics simulations. *J. Comput. Chem.* **32**, 2319–2327 (2011).
106. Qi, Y. F. et al. CHARMM-GUI Martini maker for coarse-grained simulations with the Martini force field. *J. Chem. Theory Comput.* **11**, 4486–4494 (2015).
107. Souza, P. C. T. et al. Martini 3: a general purpose force field for coarse-grained molecular dynamics. *Nat. Methods* **18**, 382 (2021).
108. Yesylevskyy, S. O., Schäfer, L. V., Sengupta, D. & Marrink, S. J. Polarizable water model for the coarse-grained MARTINI force field. *PloS Comput. Biol.* **6**, e1000810 (2010).
109. Tironi, I. G., Sperb, R., Smith, P. E. & Vangunsteren, W. F. A generalized reaction field method for molecular-dynamics simulations. *J. Chem. Phys.* **102**, 5451–5459 (1995).
110. Bussi, G., Donadio, D. & Parrinello, M. Canonical sampling through velocity rescaling. *J. Chem. Phys.* **126**, 014101 (2007).

Acknowledgements

This work was supported by the National Research Foundation of Korea (2020R1C1C1003937 and RS-2025-00513015 to D.M.; 2021R1C1C1010943 to J.M.C.).

Author contributions

D.M. conceived and supervised the project. V.W.S., S.K., and D.M. designed the single-molecule tweezer experiments. V.W.S. performed the single-molecule tweezer experiments. V.W.S., S.K., E.K., and D.M. analyzed the single-molecule experiment data. V.W.S. and S.K. purified the proteins and prepared the molecular constructs. E.K. and D.M. performed the MD simulations. E.K., T.L., J.M.C., and D.M. analyzed the MD simulation data. W.C.B.W. performed the TEM measurements. V.W.S., E.K., S.K., and D.M. prepared the manuscript with input from all authors.

Competing interests

The authors declare no competing interests.

Additional information

Supplementary information The online version contains supplementary material available at https://doi.org/10.1038/s41467-025-62852-1.

Correspondence and requests for materials should be addressed to Duyoung Min.

Peer review information *Nature Communications* thanks Yongli Zhang, and the other anonymous reviewer(s) for their contribution to the peer review of this work. A peer review file is available.